BRNO UNIVERSITY OF TECHNOLOGY
VYSOKÉ UČENÍ TECHNICKÉ V BRNĚ

FACULTY OF MECHANICAL ENGINEERING
FAKULTA STROJNÍHO INŽENÝRSTVÍ

INSTITUTE OF PHYSICAL ENGINEERING
ÚSTAV FYZIKÁLNÍHO INŽENÝRSTVÍ

MICROSCOPIC AND SPECTROSCOPIC ANALYSIS OF ELEMENTARY 2D MATERIALS
MIKROSKOPICKÁ A SPEKTROSKOPICKÁ ANALÝZA JEDNOPRVKOVÝCH 2D MATERIÁLŮ

BACHELOR'S THESIS
BAKALÁŘSKÁ PRÁCE

AUTHOR AUTOR PRÁCE	**František Jeřábek**
SUPERVISOR VEDOUCÍ PRÁCE	**doc. Ing. Miroslav Kolíbal, Ph.D.**

BRNO 2023

Assignment Bachelor's Thesis

Institut:	Institute of Physical Engineering
Student:	**František Jeřábek**
Degree programm:	Physical Engineering and Nanotechnology
Branch:	no specialisation
Supervisor:	**doc. Ing. Miroslav Kolíbal, Ph.D.**
Academic year:	2022/23

As provided for by the Act No. 111/98 Coll. on higher education institutions and the BUT Study and Examination Regulations, the director of the Institute hereby assigns the following topic of Bachelor's Thesis:

Microscopic and spectroscopic analysis of elementary 2D materials

Brief Description:

Elementary 2D materials are a new, highly attractive class of materials that exhibit unusual physical properties. However, these are challenging to analyse due to the sensititvity of these materials to atmospheric conditions. Within the bachelor thesis the student will be in charge of analysis of these materials prepared in ultrahigh vacuum utilizing microscopic and spectroscopic techniques. The work will comprise also a study of their degradation processes in oxidative environment.

Bachelor's Thesis goals:

1. Get trained in appropriate analytical techniques for analysis of physical properties of the aforementioned materials (STM, XPS, etc.).
2. Analyze structural properties and elemental composition of these materials.

Recommended bibliography:

MANNIX, Andrew J., Brian KIRALY, Mark C. HERSAM a Nathan P. GUISINGER. Synthesis and chemistry of elemental 2D materials. Nature Reviews Chemistry. 2017, 1(2), 0014. ISSN 2397-3358. Dostupné z: doi:10.1038/s41570-016-0014

ZHANG, Jia Lin, Songtao ZHAO, Shuo SUN, et al. Synthesis of Monolayer Blue Phosphorus Enabled by Silicon Intercalation. ACS Nano. 2020, 14(3), 3687-3695. ISSN 1936-0851. Dostupné z: doi:10.1021/acsnano.0c00822

Deadline for submission Bachelor's Thesis is given by the Schedule of the Academic year2022/23

In Brno,

L. S.

prof. RNDr. Tomáš Šikola, CSc.
Director of the Institute

doc. Ing. Jiří Hlinka, Ph.D.
FME dean

Abstract

This work presents an atomic-level mapping of the structures formed upon deposition of phosphorus on a Cu(111) single-crystal under ultra-high vacuum conditions. A comprehensive overview of the current advancements in the synthesis of black and blue phosphorene is provided, encompassing both experimental preparation techniques and predictions of degradation processes. The analysis employs atomically-resolved scanning tunneling microscopy and spectroscopy to examine three distinct structures characterized by varying levels of phosphorus coverage. Remarkably, this investigation succeeds in identifying a large-scale single-layer blue phosphorene. Furthermore, an in-situ examination of the stability of these structures is conducted, revealing the rapid degradation of blue phosphorene even within an ultra-high vacuum environment.

Abstrakt

Tato práce se zabývá analýzou struktur tvořených při depozici fosforu na monokrystal mědi Cu(111) za podmínek ultravysokého vakua. Součástí práce je komplexní shrnutí aktuálního pokroku v oblasti syntézy černého a modrého fosforenu. Kromě samotných metod přípravy je diskutována také předpovězená stabilita těchto struktur. V práci jsou prezentovány výsledky analýzy tří struktur pomocí skenovací tunelové mikroskopie a spektroskopie, prokazující možnost přípravy jednovrstvého modrého fosforenu na měděném substrátu. In-situ analýza stability připravených struktur pomocí skenovací tunelovací mikroskopie prokazuje velmi rychlou degradaci modrého fosforenu i za podmínek ultravysokého vakua.

Keywords

Phosphorene, 2D materials, STM, Cu(111), degradation, UHV.

Klíčová slova

Fosforen, 2D materiály, skenovací tunelová mikroskopie, degradace, UHV.

Reference

JEŘÁBEK, František. *Microscopic and spectroscopic analysis of elemental 2D materials.* Brno, 2023. Bachelor's thesis. Brno University of Technology, Faculty of Mechanical Engineering. Supervisor doc. Ing. Miroslav Kolíbal, Ph.D.

Microscopic and spectroscopic analysis of elemental 2D materials

Declaration

I hereby declare to have written this thesis on my own, under the supervision of doc. Ing. Miroslav Kolíbal, Ph.D., my bachelor's thesis supervisor. I have used no other resources except those cited and mentioned in the references.

. . . .
František Jeřábek
May 26, 2023

Acknowledgements

I hereby express my biggest thanks to doc. Ing. Miroslav Kolíbal, Ph.D. for an inspiring, friendly and encouraging guidance during the research and thesis finalization. Also, I owe my thanks to my friend and colleague Bc. Jiří David for a kind cooperation during the experimental research. Last but not least, I would like to express my biggest gratitude to my family and friends, who have supported me during my studies.

Contents

Introduction

In recent years, the study of two-dimensional (2D) materials has emerged as an exciting and promising field of research, driven by their unique and fascinating properties [1]. Unlike bulk materials, where all the three dimensions are very large compared to the atomic scale and which are composed of a large number of atoms, 2D materials are single or few-layered and, hence, only a few atoms thick. Due to their reduced dimensionality, 2D materials have a high surface-to-volume ratio and exhibit strong quantum confinement effects. As a result, they exhibit properties that are essentially different from those of their bulk counterparts, making them highly attractive for both fundamental research and potential technological applications [2].

Graphene, probably the most well-known and extensively studied 2D material, is composed of a single layer of carbon atoms showing a honeycomb arrangement. The in-plane structure of graphene is based on the strong C-C covalent bonds, while the particular sheets of graphene are connected together by means of van der Waals interactions to form graphite. The valence and conduction bands of graphene meet at the so-called Dirac point, which is located at the corners of the Brillouin zone. The electronic dispersion around the Dirac point is linear, which gives rise to unusual behavior of charge carriers, adopting properties of massless Dirac fermions. Along with a number of other interesting consequences, this gives rise to an exceptionally high charge carrier mobility [3]. The 2D materials, however, do not need to be composed of only one atom species. TMDs (transition metal dichalcogenides), for example, are a family of 2D materials composed of a transition metal atoms sandwiched between two layers of chalcogen atoms. They exhibit a range of interesting properties, including strong photoluminescence, high electron mobility, and excellent mechanical strength. Unlike graphene, the TMDs do have a finite bandgap that can be tuned by applying an external electric field or mechanical strain [4, 5]. Hexagonal boron nitride (hBN), another widely studied representative of the 2D materials family, shows a large bandgap which makes it an excellent insulator [6].

The group of 2D materials thus covers a whole range of material types showing various and often tunable properties. Large-scale industrial applications will, however, require to overcome a number challenges. As a consequence of the low dimensionality, the properties of the 2D materials are strongly dependent on the surrounding environment. Even minor defects present in the prepared materials may result into unpredictable behaviour, introducing a requirement of an absolutely clean and stable environment. In addition, the conventional methods for preparation of high-quality 2D materials represent complex, expensive and time-consuming processes which are usually resulting in products of a very limited scale and use [7]. In light of this, a major attention of the scientific community has recently been attracted to the bottom-up synthesis methods (CVD, PVD, etc.). Although being technically demanding, this approach represents a possible path to the actual industrial-scale fabrication of the 2D materials.

In this work, we focus on the atomic-level analysis of structures grown by evaporation of phosphorus on a copper crystal under ultra high vacuum. The first chapter (Theory) introduces the two most stable allotropes of 2D crystalline phosphorus (i.e. phosphorene) which are both predicted to exhibit a very high carrier mobility while showing an intrinsically present wide band gap. Furthermore, the chapter builds a systematic overview of the current state-of-the-art phosphorene synthesis, taking in consideration both the top-down and bottom-up methods. The second chapter (Methods) is dedicated to a brief introduction to the techniques used in the experimental research for this thesis, covering the methods of substrate and structure preparation and analytical microscopic and spectroscopic methods (LEEM, STM, STS). In the beginning of the third chapter (Experiment), the results of Bc. Jiří David's and Dr. Miroslav Kolíbal's in-situ LEEM growth experiments are briefly introduced in order to build the necessary background. The attention is then focused onto an atomic-level in-situ STM analysis of the grown structures carried out by the author. A successful preparation and recognition of a single layer blue phosphorene is reported, thorough study of the sub-monolayer and few-layer structures growth is also presented. Finally, an in-situ STM analysis of the blue phosphorene stability is presented.

Chapter 1

Theory

1.1 Phosphorene

Phosphorene is a highly regarded representative of the still growing family of 2D materials, especially due to its outstandingly high carrier mobility and strong light-matter interaction. These properties were predicted for both the most attractive allotropes of a two-dimensional phosphorus, the black and blue phosphorene, which differ notably both in structural and functional properties. While the black phosphorene is showing a strongly buckled armchair spatial configuration in one direction, the structure of the blue phosphorene is significantly less buckled and is represented by a characteristic zigzag pattern observable in the directions of both the in-plane lattice vectors (see Figure 1.1) [8].

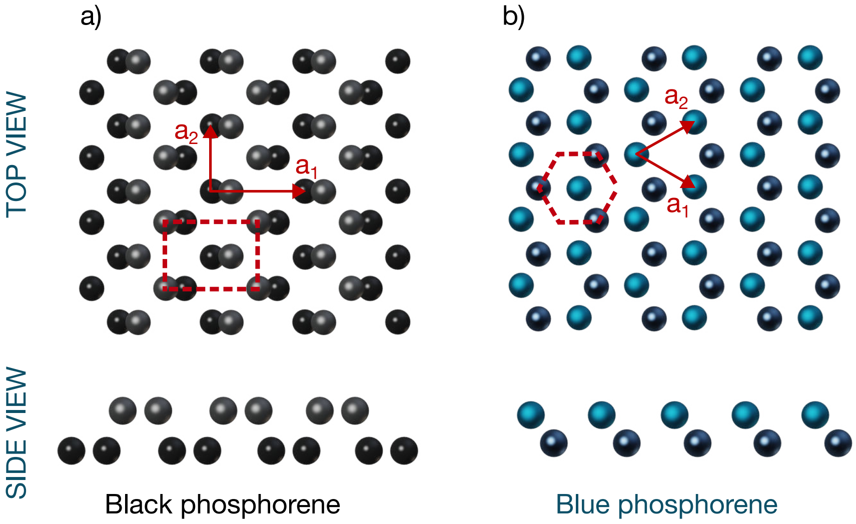

Figure 1.1: Crystal structure of (a) black phosphorene and (b) blue phosphorene. Atoms in different planes are denoted by different colors, the Wigner-Seitz unit cell (dashed red) and the in-plane lattice vectors (a_1 and a_2) are shown in the top views. Black phosphorene has a four-atom unit cell with an armchair structure along a_1 and a zigzag structure along a_2. Blue phosphorene has a two-atom unit cell with the zigzag structure along a_1 and a_2. The side views show the armchair and zigzag structures. The lattice constants are $|a_1| = 4.43$ Å and $|a_2| = 3.28$ Å for black phosphorene, and $|a_1| = |a_2| = 3.33$ Å for blue phosphorene. Adapted from [9].

In the beginning of 2014, a hundred years after the first successful synthetic preparation of its bulk version, the black phosphorus experienced a renaissance thanks to an emerging and quickly developing field of low dimensional materials research [10]. Initial computational studies predicted previously unseen properties for the new layered thin film material, including very high carrier mobility or a variable, layer-dependent and strain induced direct bandgap covering the energy range of 0.3 eV to 2 eV. In light of these exciting predictions, black phosphorene has instantly attracted a considerable attention of the experimental physicists [11, 12].

Not even a year after, the first successful experimental studies of the black phosphorene preparation were published, proving the previously predicted outstanding properties of the material. It has been shown it is possible to obtain a single or few-layer black phosphorene by means of mechanical exfoliation of bulk black phosphorus [13]. This top-down method had been previously used for the first preparation of other famous two-dimensional materials such as graphene [14] and thanks to its accessibility, simplicity and high-quality outcome, it is used till nowadays particularly in the field of research and development [15].

However, the method of bulk precursor exfoliation is generally not suitable for mass production of black phosphorene, which would be needed for any industrial application of the material. In particular, this is caused by the impossibility of the exfoliation process automation and relatively small-scale flakes of black phosphorene resulting from the technique. The method is still being developed and several enhanced subtechniques of the black phosphorene exfoliation have been discovered, including the microwave/ultrasound assisted liquid phase exfoliation or electrochemical exfoliation [16–19]. Still, the requirements for the usage of the material as a functional part of actual electronic devices generally can not be fulfilled by means of these techniques, particularly because of the need for precisely defined and large scale phosphorene sheets of a very high quality and purity. However, a whole class of preparation techniques has experienced a large expansion recently, taking a completely opposite direction to the one described above, building the desired structures from single atoms.

The field of bottom-up methods could be described as a rather physical approach to the nanostructures fabrication, using modern state-of-the-art equipment for a direct growth of pure, precise and relatively large-scale structures. However, it is still a challenge to develop appropriate experimental conditions and best practice for the particular structure preparation, since these methods are usually very sensitive even for small changes of the growth conditions.

The black phosphorene was shown to be fabricable by several methods, including the chemical vapor deposition (CVD). In 2016, Smith et al. have reported a successful deposition of large-scale black phosphorus films onto a silicon substrate using a chemical vapor deposition from amorphous red phosphorus films. However, while the few-layer black phosphorene regions were observed, their surface did not exceed 3.5 μm^2. Black phosphorus films of much larger lateral dimensions were also grown, however, the thickness of the film was already not sufficiently small to be characterised as phosphorene [20].

Interesting results were achieved by Wu et al. in 2021, who have reported a milimeter scale double-layer black phosphorene fabrication by means of pulsed laser deposition (PLD) on a mica substrate. The success of the technique is based on the creation of a localised, high temperature and high pressure laser ablation induced plasma, activating the region close to the target substrate surface, and thus bringing the necessary extreme conditions for a black phosphorene formation. However, the quality of the obtained phosphorene is still not good enough for the applications in the field of the semiconductor industry [21].

One of the most promising techniques for the large-scale and high quality crystalline black phosphorene fabrication was presented in 2020 in a work of Wu et al. Here, a direct controllable growth of a layered black phosphorus in the epitaxial mode is reported, while taking advantage of a gas phase deposition technique. The resulting structure can be tuned in terms of the number of layers as well as the horizontal dimensions, while maintaining a quality comparable with the the structures obtained by the bulk black phosphorus exfoliation processes. However, similarly to the previously mentioned PLD black phosphorus films fabrication, the true few-layer black phosphorene is obtained only on a micrometer lateral scale [22].

It is evident that black phosphorene is an intriguing material with a myriad of potential technological applications. However, the production of wafer-scale sheets that are suitable for use in the semiconductor industry presents a significant challenge. Consequently, considerable attention from the scientific community has been directed towards the second most stable crystalline allotrope of two-dimensional phosphorus - blue phosphorene. This emerging semiconductor was found to be formed in place of previously expected black phosphorene within a phosphorus on-substrate deposition under the ultra high vacuum conditions. Having no naturally occuring bulk counterpart, the blue phosphorene is exclusively producible through bottom-up methods and belongs to the family of entirely synthetic 2D materials, thereby offering the possibility of deliberate tuning of its electronic properties directly. Analogous to black phosphorene, free-standing blue phosphorene has been predicted to exhibit a wide bandgap of 2 eV. Given its non-planar structure, the electronic properties of blue phosphorene are heavily dependent on the magnitude of applied mechanical strain, which is in turn directly influenced by the type of substrate, interaction strength, and lattice constant. In light of the necessity of substrate use within the bottom-up approach, a judicious substrate selection process becomes a critical step in the preparation of blue phosphorene with the desired properties [23].

The emergence of blue phosphorene as a promising 2D semiconductor has sparked numerous computational studies aimed at identifying appropriate substrates for its epitaxial growth. According to these investigations, single-crystal noble metal substrates, such as Au(111), Ag(111), or Cu(111) have been suggested as viable options due to their reasonable lattice constant mismatch with blue phosphorene. However, density functional theory (DFT) simulations have indicated that a strong interaction between the substrate and blue phosphorene could lead to the decomposition and clustering of the phosphorene layer [23].

Zhang et al. [24] and Gu et al. [25] achieved the first successful preparations of blue phosphorene using an effusion cell loaded with bulk black phosphorus. The process involves heating of the black phosphorus, which triggers the generation of P_4 clusters forming the molecular beam. While Zhang et al. employed a clean Au(111) surface as a substrate, Gu et al. reported blue phosphorene growth on a Te monolayer functionalized Au(111) substrate. The tellurium functionalization resulted in a significant decrease in the substrate-phosphorene interaction strength, which was confirmed by DFT calculations and PES measurements. The successful synthesis of blue phosphorene on this substrate represents a promising approach for future free-standing blue phosphorene preparation. Xu et al. achieved interesting results in 2017, using a molecular beam epitaxy method with phosphorus vapor generated through InP thermal decomposition in a Knudsen cell at 470 °C. The beam is expected to consist primarily of phosphorus dimers (P_2), as previously shown using similar experimental setup [26]. Here, a formation of one-dimensional phosphorus chains as well as standard two-dimensional blue phosphorene is reported, with the obtained structure similar to the one seen in the previously mentioned works of Zhang et al. and Gu et al. A single layer blue phosphorene was recognized, showing an evident tensile strain caused by the mismatch of the Au(111)/phosphorene lattice constants. The paper describes an interesting behaviour of the phosphorus adatoms during the structure growth, with various phosphorus clusters shapes occuring (see Figure 1.2). Furthermore, a sudden phase transformation to the blue phosphorene structure is reported approaching the 1/3 ML coverage, in contrast to the continuous growth predicted by a DFT simulation. The growth was found not be spatially homogeneous, since the chain-like structure can be observed along with terraces/islands consisting of the blue phosphorene [27]. In contrast with the previously mentioned works that had presented a single full-coverage structure formation, Zhang et al. have reported observation of two structures differing in number of bright protrusions visible in the triangular features. Again, the deposition was realised using a Knudsen cell loaded with black phosphorus. While six protrusions were observed in the initial studies, this work shows the coexistence of three and six protrusions-composed triangles (see Figure 1.3) [28]. The observed structures were, however, later found to represent 2D Au-P alloy networks instead of the previously believed blue phosphorene [29]. Additional transformation of the triangular alloy structure into single-layer blue phosphorene can be done via silicon intercalation of the Au-P alloy on Au(111) surface [30].

As mentioned above, Ag(111) was also predicted to be a promising substrate for the blue phosphorene growth. Yin et al. have published a complex computational study, describing the process of several phosphorus isomers formation under the deposition on Ag(111) crystal simulated using first-principles methods. It was shown that at a low phosphorus coverage, one-dimensional armchair-shape chains are the most likely to be formed, followed by a pentameric structure dominant at a medium phosphorus coverage. Increasing the coverage, a blue phosphorene structure becomes the most probable structure to be formed [31]. The initial formation of one-dimensional chains and subsequential pentameric structure stabilisation was proven experimentally by Wang et al. just recently, along with nanoribbon-like structures and phosphorus polymers (see Figure 1.4). The blue phosphorene structure appears, however, only in a modified clusterized form, as was also previously shown in other experiments [32]. This is believed to be caused by almost a twice as high atom coverage of standard blue phosphorene compared to the two previously mentioned structures with similar stability. Furthermore, the clusterisation is believed to be supported by a relatively high Ag - P interaction strength and the lattice mismatch, even though the mismatch is considered relatively small [33].

While Au(111) and Ag(111) crystals have been the primary focus of attention as potential substrates for blue phosphorene growth, Cu(111) has received less attention from experimental scientists, likely due to the above mentioned concerns regarding potential instability of the phosphorene layer resulting from strong interactions with copper substrate. In light

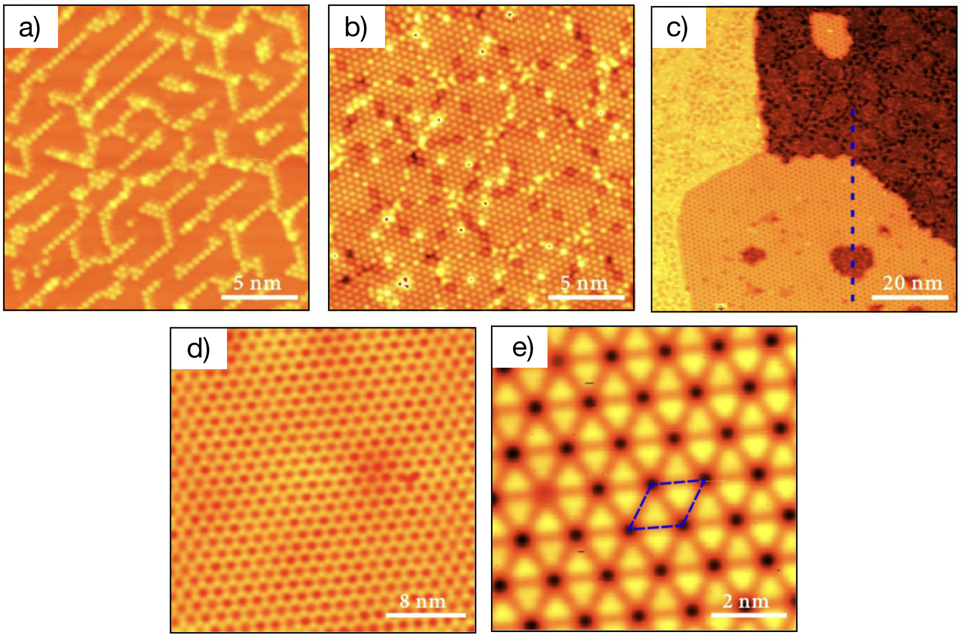

Figure 1.2: Scanning tunneling microscope images of the sample surface during the phosphorus deposition on Au(111): a) chain-like 1D phosphorus structure (image size: 20 × 20 nm^2 ; $V_{bias} = 0.1$ V): 1D chain-like patterns appear as a first structure, intersecting to form „Y-like“ shapes and mostly avoiding the formation of isotropic „star-like“ shapes, b) $(\sqrt{3}\times\sqrt{3})$R30° superstructure (image size: 20 × 20 nm^2 ; $V_{bias} = 0.1$ V), c) mixed regions of $(\sqrt{3}\times\sqrt{3})$R30° structure and blue phosphorene (image size: 80 x 80 nm^2 ; $V_{bias} = 0.1$ V), d) surface fully covered with blue phosphorene (image size: 30 × 30 nm^2, $V_{bias} = 1$ V), e) closeup image of structure shown in d) (image size: 8 × 8 nm^2, $V_{bias} = 0.1$ V). Adapted from [27].

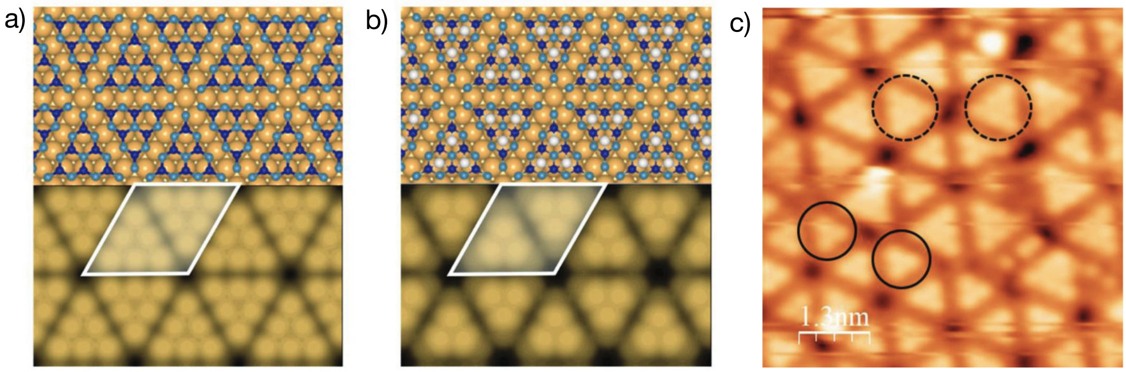

Figure 1.3: The model systems of blue phosphorene on the (5 × 5) Au(111): a) 32 P atoms forming two triangles with six bright protrusions each; the corresponding simulated STM image. b) Additional 2 × 3 P atoms on the two triangles; the corresponding simulated STM image. c) Filled state STM image corresponding to 1 ML of phosphorus on Au(111) held at 260 °C (U = -2.0 V, I = 0.44 nA). Two triangles with three and six protrusions each are highlighted by full and dashed circles, respectively. Adapted from [28].

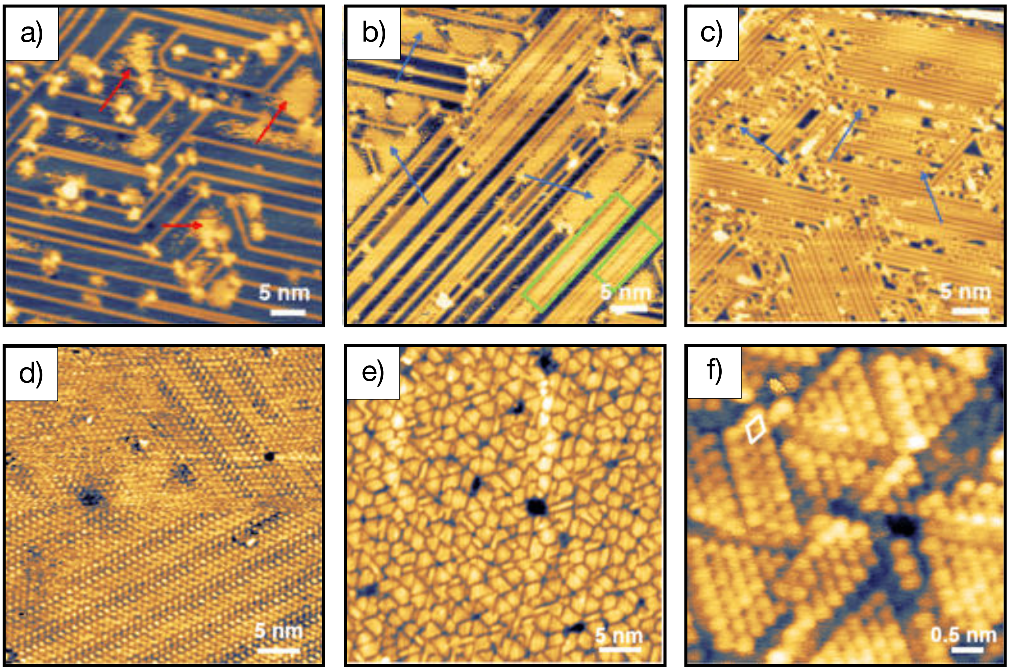

Figure 1.4: Scanning tunneling microscope images of the sample surface during the phosphorus deposition on Ag(111): a) 1D tetragonal chains formed at 0.15 ML (V_{tip} = -0.8 V, I = -100 pA, 50 × 50 nm^2); b,c) Nanoribbon-like structures and P polymers are observed at b) 0.6 ML and (c) 1.0 ML [b) V_{tip} = -0.8 V, I = -100 pA, 50 × 50 nm^2; c) V_{tip} = -1 V, I = -100 pA, 40 × 40 nm^2]; d) An ordered pentamer film obtained by annealing a 0.4 ML sample at 150 °C (V_{tip} = -0.8 V, I = -100 pA, 40 × 40 nm^2); e) Large-scale STM image of the quasi-BlueP films with a coverage of 0.8 ML and annealing at 150 °C (V_{tip} = -1 V, I = -100 pA, 40 × 40 nm^2); f) zoomed-in image of the films to resolve the atomical structure (V_{tip} = -100 mV, I = -1 nA, 6 × 6 nm^2). Adapted from [33].

of these concerns, Zhou et al. proposed a new technique involving the transformation of the copper crystal's upper layer into a thin Cu_3O_2 oxide layer prior to phosphorus deposition. This results in the creation of a honeycomb-structured buffer layer that shields the copper-phosphorus interactions. Supported by promising DFT simulations, the researchers report successful fabrication of a weakly bound blue phosphorene layer, which exhibits significantly reduced mechanical surface strain compared to structures grown on clean metal crystals. The phases observed during the phosphorus deposition and annealing can be seen in the Figure 1.5: initially the phosphorus clusters are formed on the Cu_3O_2 surface within the deposition at 350 K, being transformed into a hexagonally packed dotted structure by annealing at 450 K. Further annealing of the sample at 520 K leads to the formation of blue phosphorene showing irregular moire pattern in the STM. When deposited on the oxide layer containing defects, the phosphorus atoms adopt a modified arrangement characterized by clusters showing a dimeric zig-zag pattern (see Figure 1.6) [34].

Very recently, Kaddar et al. published a paper reporting a successful growth of the blue phosphorene on bare Cu(111) using a MBE technique realised with bulk black phosphorus precursor loaded Knudsen cell. Here, analytical techniques including the Low energy electron diffraction in combination with Scanning tunneling microscopy/spectroscopy and

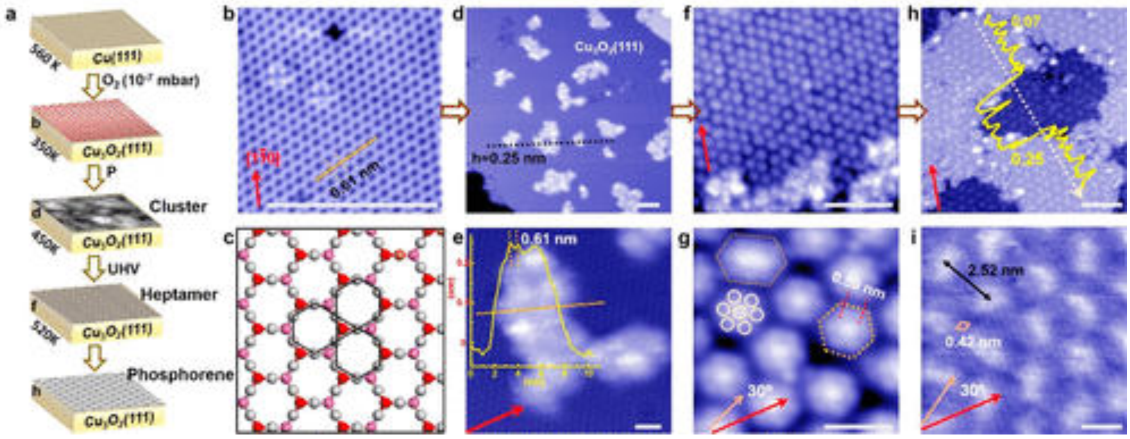

Figure 1.5: Growth of flat phosphorene on copper oxide. (a) Schematic of the evolution process from P cluster to phosphorene. (b) Atomic-resolution STM image of Cu_3O_2 film on Cu(111). The arrow indicates the [110] direction of the substrate. (c) Ball and stick model of the $Cu_3O_2(111)$ surface. White, pink, and red balls represent Cu atoms and O atoms in the bottom and top planes, respectively. (d) P clusters with an average height of 0.25 nm after deposition on Cu_3O_2/Cu(111) at 350 K. (e) Zoomed-in image showing the individual P atoms within the cluster. (f) Hexagonally packed dot arrays formed after annealing at 450 K. (g) Atomically resolved STM image showing the configurations of the dots in (f). (h) Formation of large-scale phosphorene after annealing at 520 K for 30 min. (i) High-resolution STM image of the phosphorene with irregular Moiré pattern. Scanning parameters: (b,d,e) 2 V, 100 pA; (f) 1 V, 100 pA; (g) 1 V, 1 nA; (h) -1.2 V, 100 pA; (i) 1 V, 500 pA. Scale bars: 10 and 2 nm for top and bottom panels, respectively. Adopted from [34].

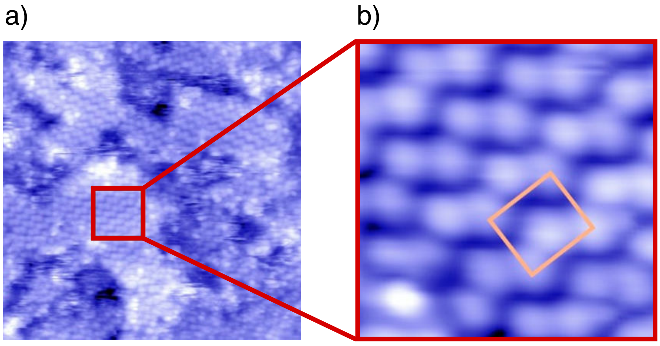

Figure 1.6: Growth of phosphorene on copper oxide with defects. Formation of zigzag chains after phosphorus deposition at 350 K and subsequent deposition annealing at 450 K.: a) large-scale image showing the zigzag pattern on top of the phosphorus clusters. The scale bar is 5 nm wide; b) Close-up image showing the dimer pairs in the zigzag pattern. A rectangular unit cell is labeled. The acquisition parameters are same for both of the images with bias voltage of 2.8 V and setpoint of 55 pA. Similar structure is observed in the experimental part of this work, see Section 3.2.3 and Summary. Adapted from [34]

Angle resolved photoemission spectroscopy are used to characterize the grown structures. It is reported that the deposition of 1 ML of phosphorus atoms onto a Cu(111) surface held at 260 °C leads to the formation of phosphorene showing a moire effect coming from the substrate-phosphorene lattice mismatch, observable both with LEED and STM, carrying the spatial period of 4.3 nm. Further deposition is reported to result into the formation of phosphorus nanodots over the previously formed phosphorene monolayer, aligned with the Cu(111) crystallographic axes. The observed nanodots show a lattice constant of 3.3 nm and the resulting structure is thus characterized as (13×13). According to the STS and ARPES results, the obtained blue phosphorene monolayer shows metallic properties, similarly to the blue phosphorene grown on the Cu_3O_2 substrate [34]. In contrast to the bare monolayer, the next structure containing the phosphorus nanodots placed over the phosphorene monolayer shows a 0.5 eV wide bandgap. Both phases were shown to adopt a linear dispersion, pointing out the existence of Dirac fermions in the grown structure [35]. Despite the remarkable results presented in the work of Kaddar et al., serious inconsistencies were observed including nonmatching dimensions of scalebars and line profile measurements. Reported results thus cannot be considered relevant for interpretation of the experimental results.

As can be seen, various and often contradictory results were reported both in the field of the blue phosphorene growth experiments and computational studies. This inconsistency throws the actual growth and analysis experiments results into doubt, encouraging further systematic and detailed research in the field. In addition, phosphorene was predicted to undergo strong degradation processes whose understanding is crucial for any future industrial application of the material [36]. Studying of the grown structures stability in various environments thus becomes an important field of research, introducing another variable into the future phosphorene fabrication methods development.

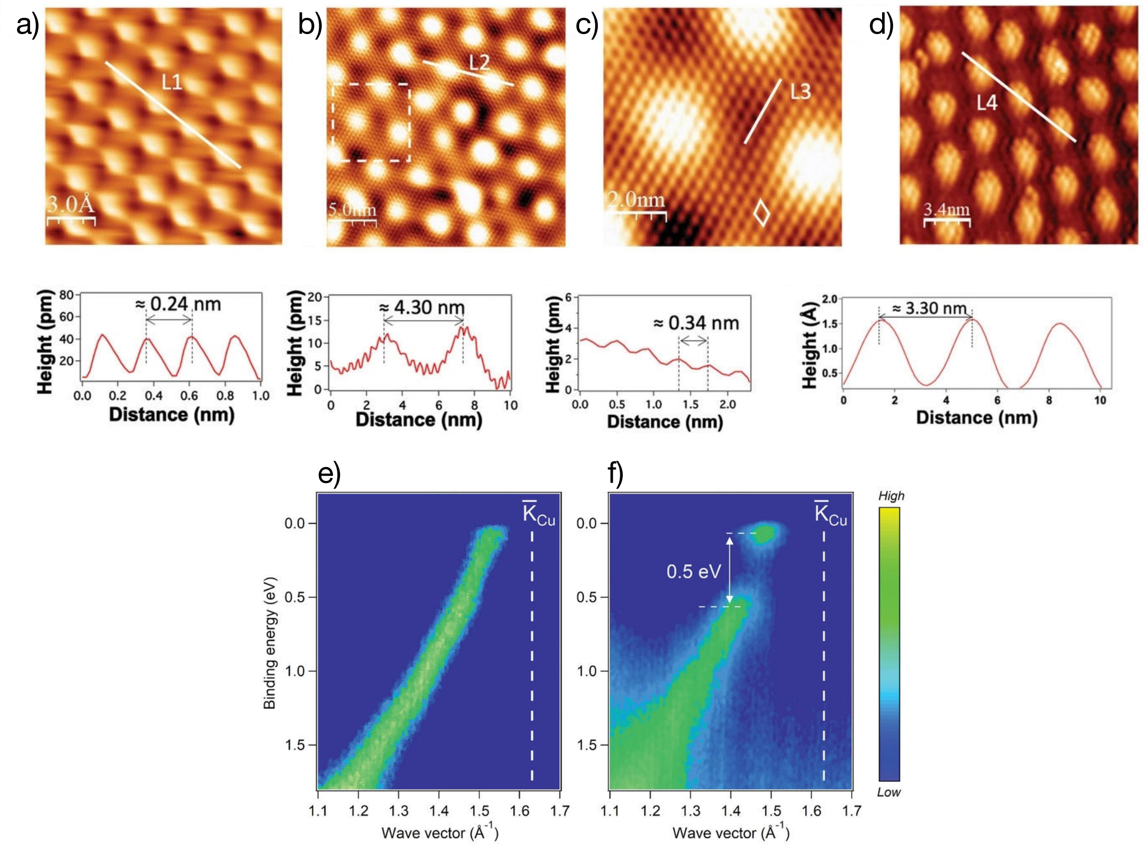

Figure 1.7: Blue phosphorene growth on bare Cu(111). Similar structures are observed in the experimental part of this work, although showing different dimensions than reported by Kaddar et al. (see Chapter 3.2.2). However, the size of features reported in the following images does not match the dimensions defined by the included scalebars and thus is not suitable for a relevant comparison. Atom resolved STM images: a) image corresponding to the bare Cu(111), U = -0.1 V, I = 3.3 nA, line profile along the line L1; b) image recorded after deposition of 1 ML of phosphorus atoms, U = -0.01 V, I = 2.5 nA, line profile recorded along the line L2; c) image corresponding to the square in b), U = -0.01 V, I = 2.5 nA, line profile recorded along the line L3; d) image recorded after deposition of 1.5 ML of P atoms on Cu(111), U = -1 V, I = 1 nA, line profile recorded along the line L4; HR-ARPES measurements recorded along the Γ - K direction at 57 eV photon energy: e) Linear dispersion observed after deposition of 1 P ML (phosphorene adlayer). f) Bandgap opening after deposition of P nanodots on phosphorene adlayer. Adapted from [35].

Chapter 2

Methods

2.1 Ultra-high vacuum cluster

Generally, the bottom-up methods for precise 2D structures preparation require the finest and cleanest substrate surface possible and a non-reactive environment with a minimal amount of contamination sources. Similar conditions are usually needed by the analytical techniques that are suitable for characterisation of the structures. This naturally leads to the usage of the vacuum techniques.

This being said, the preparation and characterisation of phosphorene requires the use of a state-of-the-art ultra high vacuum (UHV) equipment, allowing the substrate preparation, phosphorene synthesis and a whole analysis procedure without leaving the UHV conditions.

The whole procedure of the experimental research was thus held in the Nanocharacterisation laboratory of the CEITEC nano facility, using the complex set of instruments combined in a single ultra high vacuum cluster. As can be seen in the Figure 2.1, the cluster consists of nine UHV chambers dedicated to the particular fabrication or analytical techniques, connected by a magnetically driven linear transfer system. The whole cluster, including the actual transfer chamber, is maintained at the pressure of 10^{-10} mbar and, in addition, each chamber is equipped with a separation valve, allowing it to be operated or vented independently on the rest of the cluster.

2.2 Preparation methods

2.2.1 Sample cleaning procedure

To be able to prepare the desired 2D structure while preserving the reference value of the process for the best practice development, it is crucial that the substrate surface is the cleanest, finest and most homogeneous possible. In order to ensure consistent initial conditions for all further experiments, a standard substrate preparation procedure was developed, consisting of Ar ion sputtering and annealing cycles under UHV conditions. The precise procedure workflow can be found in the Table 2.1.

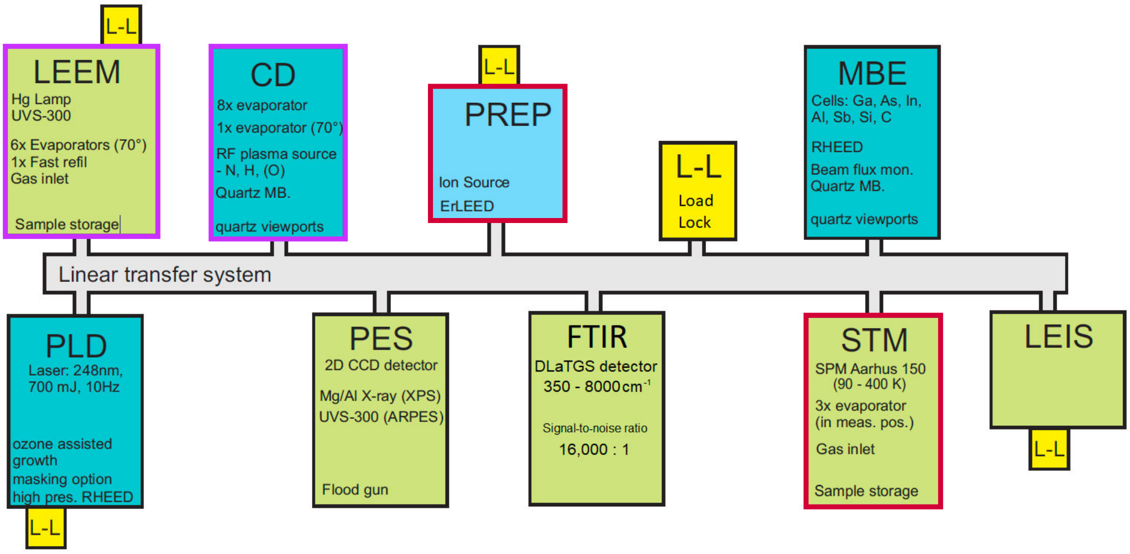

Figure 2.1: UHV cluster located in the CEITEC nano facility, Brno, Czech Republic: Besides being equipped with five loadlock chambers securing the sample insertion and withdrawal processes, the system features two dedicated deposition chambers (labeled CD and MBE). These chambers are equipped with various deposition cells and evaporators, other tools include RF plasma source or Reflection High Energy Electron Diffraction (RHEED) instrument for an immediate structure growth feedback. In addition, the Pulsed Laser Deposition (PLD) can be done as well, again in a dedicated chamber. The preparation chamber (PREP) features an Ar ion source as well as a tungsten filament heated sample manipulator, allowing the development of a standard sample cleaning procedure. The sample surface condition can be reviewed by an embedded Low Energy Electron Diffraction (LEED) instrument. The cluster also offers five chambers featuring different instruments suitable for the characterisation of the prepared samples, such as Low Energy Electron Microscope (LEEM), Photoemission Spectroscope (PES), Fourier Transform Infrared spectroscope (FTIR), Scanning Probe Microscope (SPM) and Low Energy Ion Scattering spectroscope (LEIS). Some of the analytical chambers including the LEEM, SPM or FTIR chamber allow an additional installation of a deposition cell, providing the possibility of the in-situ analysis of the growing structure. The chambers and instruments used for the experimental part of this work are highlighted with red, instruments used by Bc. Jiří David for the preparation of the analysed samples are marked with the purple frames. Adapted from [37].

2.2.2 Evaporation

As can be seen in the Chapter 1.1, the Molecular beam epitaxy (MBE) is a powerful technique suitable for the blue phosphorene epitaxial growth on various substrates. A GaP decomposition phosphorus cell (MBE-Komponenten DECO) was selected as the phosphorus source for all our experiments, particularily due to its ability to produce a high-purity P_2 beam (the P_2:P_4 ratio is reported to be about 150:1 [38]) of a finely tunable flow. As can be seen in the Figure 2.2, the evaporator is equipped with a PBN cap intended for the residual Ga atoms trapping. Although being simple, this design assures generation of a very pure P_2 beam, where the Ga flux is more than three orders of magnitude lower than the flux of

Table 2.1: Cu(111) substrate preparation procedure: the table represents an overview of one preparation cycle, which is to be repeated multiple times depending on expected level of initial substrate contamination. T_{pyro} indicates the temperature (determined using a high temperature pyrometer, emmisivity set to 0.1) at which the sample is maintained for the time specified as t_{stable}. The $t_{rampoff}$ refers to the time of the controlled sample cooling ($T_{pyro} \implies T_{threshold}$, where $T_{threshold} = 349°C$ is the minimal temperature measurable by the pyrometer). The surface cleanliness may be checked using LEED (integrated in preparation chamber).

Cu(111) substrate preparation procedure (1 cycle)					
Process	**Parameters**				
1. Annealing	T_{pyro} [° C]	t_{stable} [min]	$t_{rampoff}$ [min]		
	500	5	3		
2. Sputtering	Gas type	E [keV]	I [mA]	$p_{sputter}$ [mbar]	$\varphi_{sputter}$ [°]
	Ar 5.0	2,0	10	$1{\cdot}10^{-5}$	23
3. Annealing	T_{pyro} [° C]	t_{stable} [min]	$t_{rampoff}$ [min]		
	500	5	3		
4. Sputtering	Gas type	E [keV]	I [mA]	$p_{sputter}$ [mbar]	$\varphi_{sputter}$ [°]
	Ar 5.0	2,0	10	$1{\cdot}10^{-5}$	23
5. Annealing	T_{pyro} [° C]	t_{stable} [min]	$t_{rampoff}$ [min]		
	500	5	20		

phosphorus atoms. This is supported by the fact that no Ga contamination was detected in our samples neither using XPS, nor LEIS.

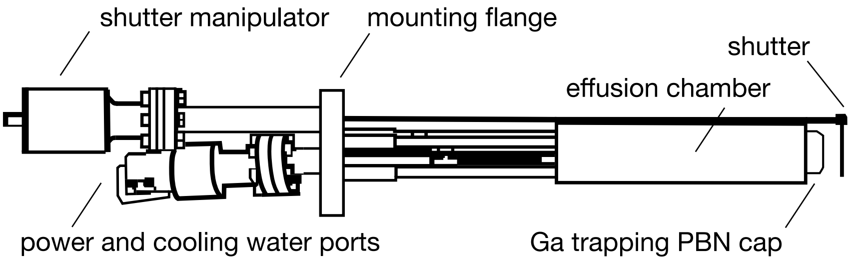

Figure 2.2: Schematic of the MBE-Komponenten DECO GaP decomposition phosphorus source. Thanks to the PBN gallium trap, the cell provides a highly pure phosphorus molecular beam composed mainly of P_2. Adapted from [38].

2.3 Analytical methods

2.3.1 Low energy electron microscopy

Low Energy Electron Microscopy (LEEM) is a powerful analytical technique that uses low energy electrons to acquire highly surface sensitive images of various samples. At first glance, the basic principle and structure of the instrument is similar to the conventional Transmission Electron Microscope (TEM). Both the electron microscopy methods make use of the true imaging mode based on a sample irradiation by a broad electron beam, unlike within the scanning mode used for example in the Scanning Electron Microscopy (SEM) or Scanning Transmission Electron microscopy (STEM). A direct comparison of the two techniques can be seen in the Figure 2.3, showing a schematic description of the instruments.

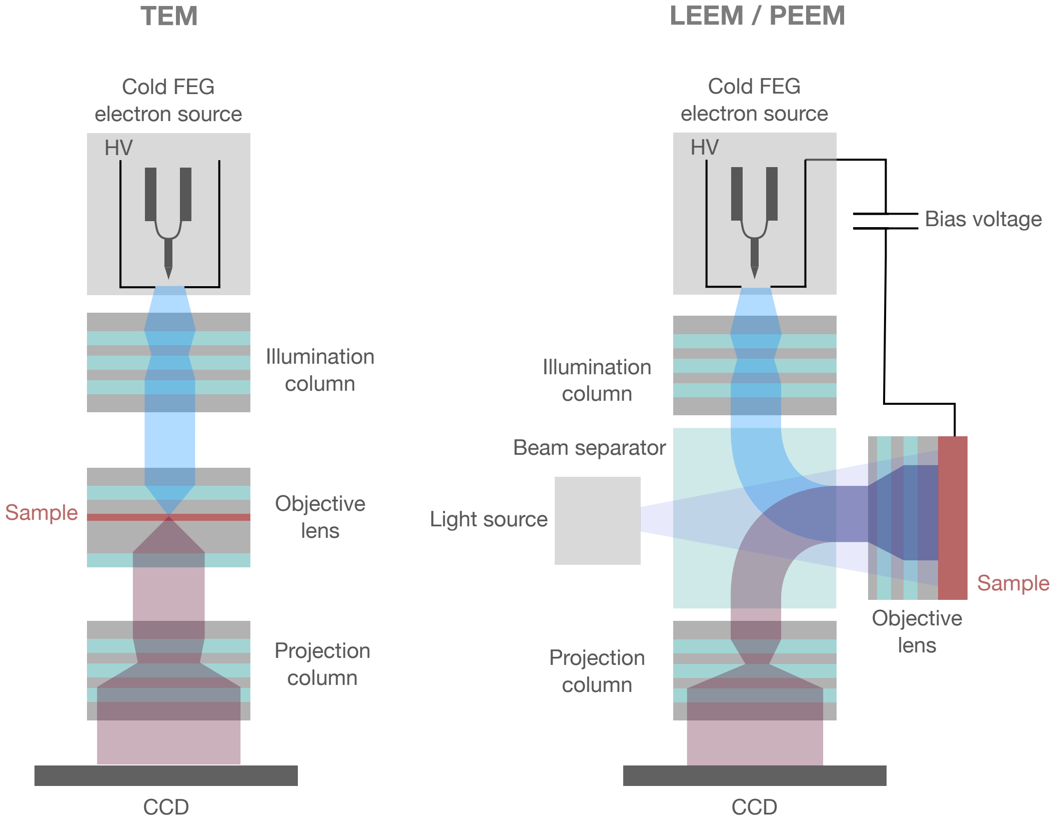

Figure 2.3: Simple construction scheme of a Transmission electron microscope (TEM) in comparison with a Low energy electron microscope (LEEM)

In LEEM, an electron source (typically cold field emission gun) is used to generate high energy electrons and direct them into the illumination optics column. Here, the electron beam is being shaped and redirected using a set of electrostatic and magnetic lenses. The resulting aberrations are being suppressed using various elements of particle optics such as stigmators (electromagnetic quadrupoles or octopoles). Leaving the illumination column, the beam enters a bending magnet and, being directed to the objective lens, it hits a conductive sample that itself represents one of the objective lens electrode. The sample is held on a high negative voltage, forcing the incoming electrons to decelerate before the actual incidence. The incident electrons thus carry relatively low kinetic energy resulting from the difference of the acceleration voltage and sample bias voltage.

The electron-matter interaction processes applying for the low-energy electrons show a significant difference compared to the high-energy-related processes. Not only the penetration depth is radically smaller bringing the characteristic high surface sensitivity of the LEEM technique, but many of the basic interaction model principles do not apply in the field of

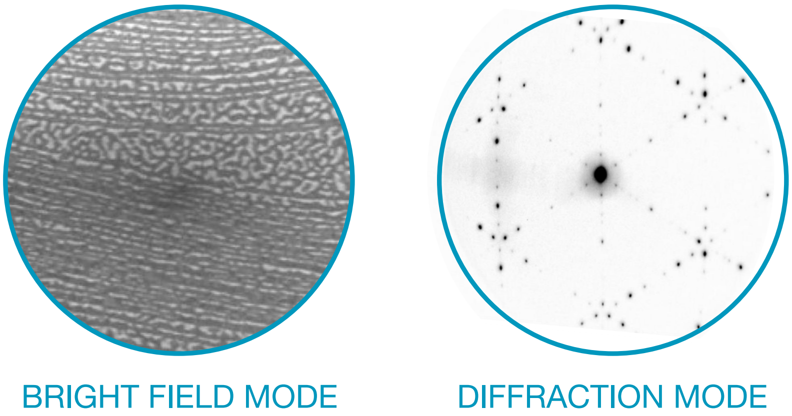

Figure 2.4: Example of images acquired using two main acquisition modes in LEEM: Bright field mode (direct space imaging) and diffraction mode (reciprocal space characterization). Switching between the modes is performed via the projection lens excitation.

low energies, leading to the impossibility to apply several traditionally used approximations. For example, the first Born approximation for the elastic scattering cannot be used since with the decreasing energy of the incident electrons, the inelastic scattering and elastic backscattering importancy increases and these processes cannot be disregarded. The inapplicability of this and some of the other high-energy-related approximations, however, results into unique properties and capabilities of the technique.

The dominant acquisition signal in LEEM originates from a very strong elastic backscattering process, while its rate depends upon the nuclear charge and the energy in a non-monotonic manner. Along with number of different complex mechanisms, the contrast is strongly influenced by the work function of the analysed sample.

Leaving the sample, the reflected electrons travel back to the beam separator, which is in case of our tool realised as a 180° deflector. Then the beam, shaped by the electromagnetic lens of the projection column, is directed towards an electron detector. Depending on the projection lens excitation, either the direct space image occurring in the objective lens image plane or the diffraction pattern located in the back focal plane is projected onto the detector surface (see Figure 2.4). This allows to obtain a complex knowledge about the topological and structural properties of the sample surface [39].

2.3.2 Scanning tunneling microscopy and spectroscopy

The general method of Scanning probe microscopy (SPM) has become one of the fundamental analytic techniques for modern nanoscale experimental physics research[40]. If well understood and handled, it provides a scientist with various information about topological, electrical and chemical properties of the sample. This being said, the SPM represents a powerful multi-purpose tool not only for the novel two-dimensional materials characterisation. As was first shown in 1990 by Eigler and Schweizer at IBM, the technique is also able to modify the surface intentionally and create desired structure [41].

In general, the scanning probe microscopy may be divided into two categories according to basic function principle and probe type – the Atomic force microscopy (AFM) and the

Scanning tunneling microscopy (STM). In the experimental research for this thesis, the scanning tunneling microscopy was used as one of the techniques for the surface analysis, the attention will thus now be focused on this method.

The fundamental principle of the theoretical model describing the contrast acquisition in STM is a pure quantum effect of tunneling. The simplest model suitable for the description of the situation in the STM is a de Broglie wave impacting a finite height square potential barrier. Here, the barrier is the vacuum gap between the sample and the probe. Let $\psi(z)$ be a representation of the incident wave. The probability density function of the wave detection behind the barrier can then be expressed in form of Equation 2.1. Here, κ is defined in Equation 2.2, d is the sample-tip distance (barrier width), A is a normalization constant. In Equation 2.2 m_e is electron mass, $\hbar$ is reduced Planck constant, $U_{barrier}$ is the potential barrier height and $E_{electron}$ is energy of the electron incident to the barrier. The current of electrons flowing between the tip and the sample is then proportional to the tunneling probability (characterized by the Equation 2.1) and the local density of states (LDOS) [40].

$$|\psi(z)|^2 = Ae^{-2\kappa d} \tag{2.1}$$

$$\kappa = \sqrt{\frac{2m_e(U_{barrier} - E_{particle})}{\hbar^2}} \tag{2.2}$$

A basic scheme of a scanning tunneling microscope construction is shown in the Figure 2.5. The key component is an extremely sharp metal tip (ideally featuring a single atom at the very tip), mounted on a manipulator – a tube with piezoelectric properties equipped with electrodes. A bias voltage is applied between the conductive sample and the tip, then the tip is slowly approached towards the sample surface using a piezoelectric actuator. A current of the electrons flowing through the gap between the tip and the surface is carefully monitored, serving as a crucial parameter for surface-tip proximity determination. Once the current reaches a predefined critical value, the approaching procedure is stopped, maintaining the gap of 0.5 to 1.0 nm between the tip and the sample. The tool is now ready for the measurement.

The microscope can be operated in two general modes - a constant height or a constant current mode. In the first one, the tip is only moving in in the xy plane, maintaining a constant z coordinate value. At each point $[x, y]$, a tunneling current is measured and recorded, providing a 2D matrix of $I(x, y)$. The second – constant current mode is based on continuous updating of the z position within a feedback circuit to fulfill the condition of a previously set constant tunneling current (i.e. setpoint). At first glance, this approach leads to the acquisition of the sample topography data. However, due to the basic principles of the tunneling effect, the tunneling current is proportional to the density of states (DOS). This being said, spots on the sample showing different electrical properties compared to the rest of the area may induce a varying tunneling current even in case of a perfectly flat surface. This naturally results in an artifact in the obtained heightmap. The topographic data of $z(x, y)$ thus can not be interpreted without taking other conditions into consideration. Furthermore, as is shown in Equation 2.3 that comes from a little more complex model of tunneling (Bardeen model), the tunneling current is characterized by a convolution of the DOS's of the sample (ρ_{sample}) and the tip (ρ_{tip}). Here, ρ_{tip} (resp. ρ_{sample}) is the density of states in the tip (resp. sample), V is the bias voltage and T represents a transmission coefficient for the vaccum barrier of thickness d. As a consequence, condition and electronic properties of the tip show an equally great influence on the resulting image. This is why the tip condition is usually desired to stay unchanged during the whole measurement.

The fact that the tunneling current is proportional to the DOS of the sample makes possible to perform mapping of this important quantity. This is done simply by measuring the tunneling current at different bias voltages while maintaining a constant surface-tip distance. The method is called Scanning tunneling spectroscopy (STS) (or Bias spectroscopy). Since the obtained signal is very weak and thus prone to various types of interference, a lock-in amplifier is usually employed in order to make the measured data interpretable. As Equation 2.4 suggests, the product of the DOS's is proportional to the dI/dV function. This is why the bias spectra are usually presented in the form of dI/dV(V) curves.

$$I = \frac{4\pi e}{\hbar}\int_0^{eV} \rho_{tip}(\epsilon - eV)\rho_{sample}(\epsilon)T(\epsilon, V, d)d\epsilon \tag{2.3}$$

$$\frac{dI}{dV} = \frac{4\pi e}{\hbar}\rho_{tip}(\epsilon - eV)\rho_{sample}(\epsilon)T(eV, V, d)d\epsilon \tag{2.4}$$

For the experimental part of this work, the Specs Aarhus 150 instrument was used for the STM measurements. Equipped with the Specs KolibriSensor quartz probe, the instrument is capable of a combined STM and Frequency modulation AFM (FM-AFM) measurement. However, the FM-AFM method outcome was found to be very probe-condition sensitive and not appropriate for the current phosphorene structures analysis. The probe was thus used solely in the STM mode.

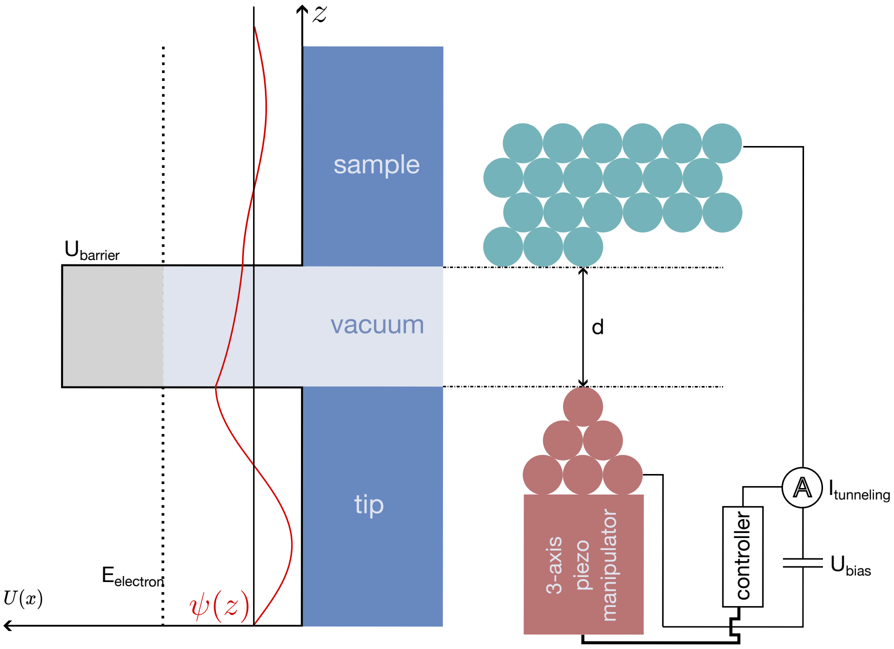

Figure 2.5: Scanning tunneling microscope: basic principles scheme. On the left, an illustration of the finite height ($U_{barrier}$) square potential barrier model is shown. The barrier represents the vacuum gap between the tip and the sample.. As can be seen, the de Broglie wave (electron) $\psi(z)$ decays exponentially within the barrier, which applies also for the probability density function $|\psi(z)|^2$. At boundary of the barrier of thickness d, the $|\psi(z)|^2$ does still show a nonzero value, allowing the electron to appear behind the barrier.

Chapter 3

Experiment

Utilizing the techniques elucidated in the preceding chapter, we executed mapping of the structures that arise during the deposition of phosphorus onto a Cu(111) single crystal. The author's emphasis lays predominantly on scanning tunneling microscopy (STM) analysis of the synthesized superstructures. However, the primary outcomes from the low-energy electron microscopy (LEEM) measurements carried out by Bc. Jiří David have also been included to construct a comprehensive understanding of the issue at hand.

3.1 Prepared superstructures

In order to systematically observe the phosphorus superstructures formation, in-situ LEEM analysis was performed. The phosporus was deposited by evaporation from GaP decomposition cell directly inside the LEEM chamber to allow real time observation. The Figure 3.1 shows a systematic overview of the phosphorus superstructures formation during in-situ LEEM analysis. The initial state is represented by the bare Cu(111) surface prepared using the standard cleaning procedure defined in the Section 2.2.1. The findings of both the diffraction and bright-field mode acquisitions are congruous with the anticipated outcomes, with the bright-field images showing the presence of large homogeneous copper terraces. During first 25 minutes following the deposition initiation, first superstructure formation is being observed. The structure (further referred to as 1st structure) exhibits diffraction pattern as shown in the corresponding image, the bright-field image shows occurrence of high-contrast domains covering the terraces of the substrate. Another 1 minute of deposition leads to a sudden transformation to another superstructure (2nd structure) showing a diffraction pattern with hexagonal symmetry and a low-contrast bright-field image. However, while the whole surface seems to be covered by a structure resulting in the homogeneously dark bright-field image, the previously seen domains are still visible as a background of the dark surface. Further deposition does not bring any immediate structural changes in the sample. Long deposition, however, leads to a continuous growth of bright quasi-triangular islands and dark clusters visible in the bright-field mode at 7 eV (3rd structure). The formation of such features on top of the 2nd structure starts approximately 90 minutes after the deposition initiation, continuing evaporation results in a slow lateral growth of the islands. A new star-like diffraction pattern is observed after 180 minutes following the deposition initiation, the bright field shows fully developed triangular islands and phosphorus clusters as shown in the corresponding image of the Figure 3.1. During the whole experiment, the sample is held at a temperature of 180 °C by the use of a tungsten filament heater embedded in the sample holder. The temperature is monitored with a pyrometer with the sample reflectivity parameter set to the standard value of (0.1). As will be shown below, the deposition at a higher sample temperature leads to the growth of quasi-triangular islands of larger lateral dimensions in contrast with a significant decrease in the dark cluster occurrence.

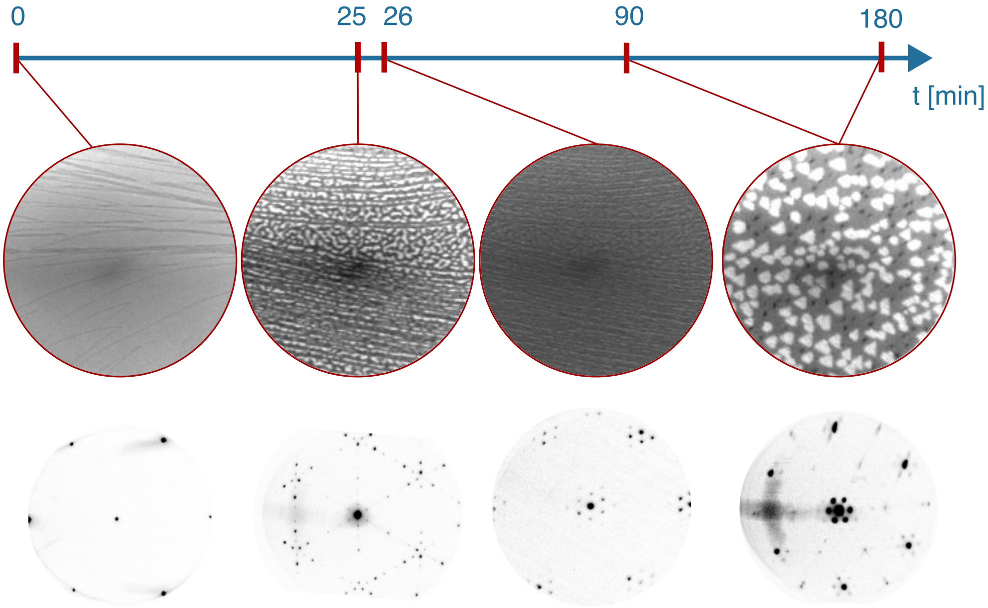

Figure 3.1: In-situ LEEM documentation of the growth experiment ($T_{sample} = 180°C$): The initial state is represented by the bare Cu(111) crystal. The bright-field image (6 eV, FOV 5 μm) shows large homogeneous terraces forming the crystal surface, the diffraction pattern corresponds to the expected one. The phosphorus deposition is initiated with the crystal held at the temperature of 180 °C. During 25 minutes, the diffraction pattern of the first superstructure is observed, the bright-field image (7 eV, FOV 5 μm) shows the existence of high-contrast domains on top of the Cu(111) terraces. Upon further evaporation, the structure undergoes a sudden transformation to another structure, with the particular bright domains in the bright-field image switching to a dark low-contrast structure. The whole transformation process is finished approximately after 1 minute of continuous deposition. The resulting structure shows a homogeneous low-contrast dark image in the bright-field mode (7 eV, FOV 5 μm) with the 1st structure domain contours visible in the background. The diffraction pattern shows a high symmetry with new hexagonally arranged spots occuring around the base spots. Further evaporation leads to the formation of new structures on top of the homogeneous 2nd structure (observed approximately 90 minutes after the deposition initiation): the bright-field image (7 eV, FOV 5 μm) shows slowly laterally growing quasi-triangular islands of high contrast and dark narrow clusters growing on top of the whole surface. At approximately 180 minutes following the deposition initiation, a star-like pattern appears in the diffraction mode image in addition to the pattern of the 2nd structure.

3.2 Detailed analysis of the phosphorus structures

To understand better the structural properties of the phosphorus structures, a detailed analysis using STM was performed in every step of the growth progress separately. In order to discover the electronic properties of the structures, attempts to perform tunneling spectroscopy measurements were made as well.

3.2.1 1st structure

Figure 3.2 shows STM images acquired on the 1st structure. In Figure 3.2a, a very low-coverage modification of the 1st structure can be seen – this linear nanochain-like structure was observed after heating the bare Cu(111) sample with closed effusion cell shutter and probably is caused by the redeposition of the residual phosphorus atoms previously deposited on the sample holder. A large-scale STM image of the standard 1st structure prepared by the process defined in the preceding chapter can be seen in the Figure 3.2b. A linear nanochain-like structure is observed, arranged in three preferred directions. The domains of this highly ordered structure are covered with an amorphous layer of phosphorus disrupted by pathways containing the nanochain-like structure. Figure 3.2c depicts a close-up view of the border between the amorphous layer and the nanochain-like structure. The line profile measurements along lines 1 and 2 in the subfigures a) and c) show that each structure has a different inter-chain distance, with the redeposited structure exhibiting a larger periodicity compared to the standard one.

Analysis of the diffraction pattern (not part of this work) corresponding to the standard 1st structure suggests the coexistence of three different superstructures, as indicated in the Figure 3.3a. The structure characterized with the smallest lattice (L1) shows the inter-chain distance of (7.74 ± 0.13) Å, which corresponds well with the pattern observed in the standard 1st structure STM measurements with the inter-chain distance of (7.9 ± 0.2) Å (presented in the Figure 3.3bc)).

3.2.2 2nd structure

Typical large-scale STM images of the 2nd grown structure are presented in the Figure 3.4: large terraces covered with a homogeneous structure exhibiting moire effect are observed. The height of the step between the terraces (peak-to-peak method measurement) was determined to (1.93 ± 0.10) Å. The step height determination process involved analysis of six different 2nd structure samples, taking into account the results obtained with different acquisition settings (bias voltage, setpoint current) since the obtained topological characteristics were proven to be independent of it. The obtained value corresponds well with the height of terraces observed by STM analysis of the bare Cu(111) crystal surface of (2.03 ± 0.04) Å. The Cu(111) crystal was treated with the standard cleaning procedure (defined in the Section 2.2.1) prior to the STM measurements. By means of statistical processing of data obtained in six STM measurement sessions with separately prepared samples, the distance between the centers of the signal maxima in the observed moire pattern was determined to (2.7 ± 0.2) nm.

Figure 3.5 shows an atomically resolved STM image showing a detailed view of the 2nd grown structure. The surface seems to be evenly covered with a well arranged superstructure corresponding with the expected appearance of the blue phosphorene. Note the local signal maxima in the image are related to the location of the upper atoms in the buckled zigzag

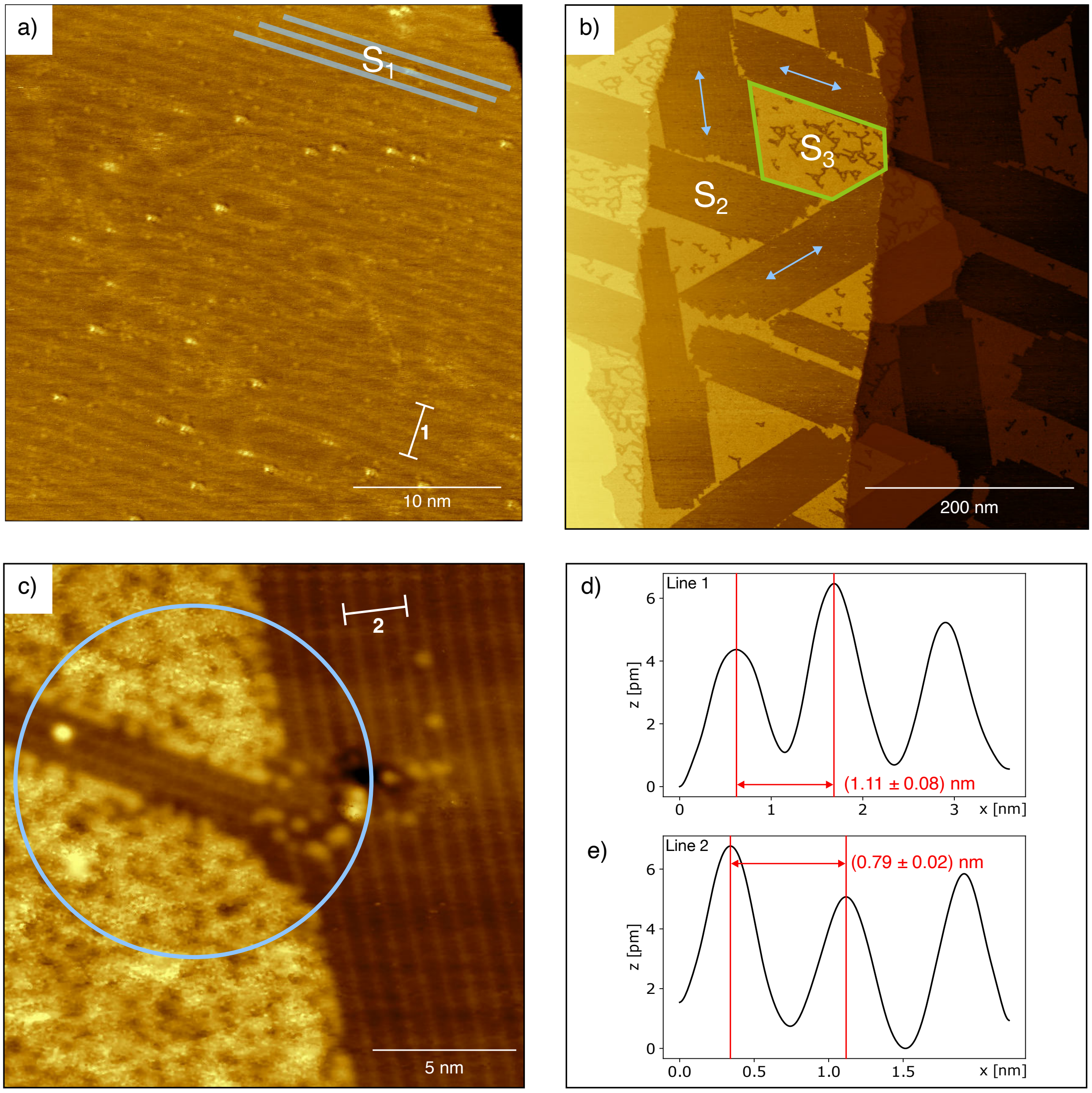

Figure 3.2: STM images of the low-coverage phosphorus structures on Cu(111): a) linear nanochain-like structure (S_1) formed upon deposition with closed effusion cell shutter ($U_{bias} = 1.7$ V, $I_{setpoint} = 50$ pA); b) large-scale image of structure grown during first 25 minutes of deposition and simultaneous sample annealing at 160 ° C: visible large regions with linear nanochain-like structure (S_2) similar to (S_1) are observed, ordered in three preferred directions (blue arrows). Amorphous clustered layer with linear paths containing the nanochain structure can be seen on top of the surface (example region highlighted with green shape) ($U_{bias} = 2.22$ V, $I_{setpoint} = 50$ pA); c) detailed image of the structure shown in b): nanochain-like structure protruding into the amorphous layer can be seen ($U_{bias} = 2.26$ V, $I_{setpoint} = 50$ pA); d) line profile along the line 1 in a); e) line profile along the line 2 in c): The nanochains formed in a) show a larger inter-chain distance than the ones formed upon a more intense deposition in b) and c).

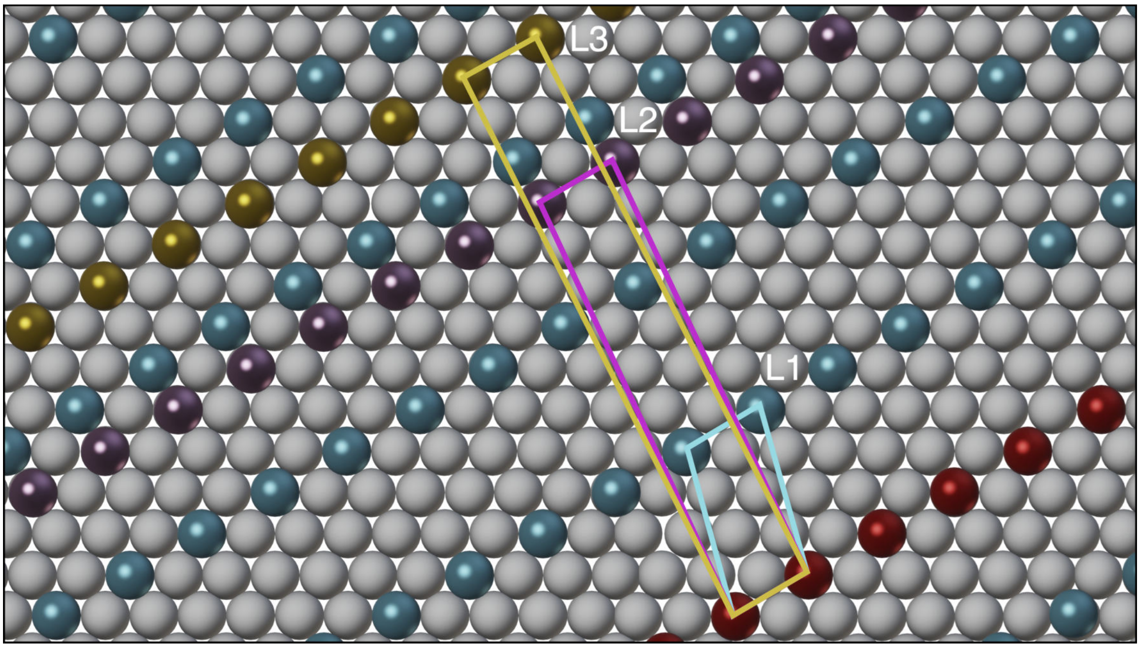

Figure 3.3: Modelled structures corresponding to the diffraction pattern of 1st structure: the blue, purple and yellow spheres represent the phosphorus atoms forming the resolved structures, the brown spheres correspond to the Cu(111) substrate surface atoms. Three 2D structures with different surface lattices (L1,L2,L3) were distinguished analyzing the previously shown diffraction pattern (not part of this work). The distance d_{th} between chains in the $(\sqrt{3}\times\sqrt{13})$R30° structure labeled L1 corresponds with the inter-chain distance d_{ex} found from the STM images of the standard 1st structure. The value of d_{th} was calculated considering the geometrical relations and the Cu(111) surface lattice constant of (2.21±0.04) Å [42] and determined to be $d_{th} = (7.74 \pm 0.13)$ Å. The value agrees with the experimentally determined value of $d_{ex} = (7.90 \pm 0.20)$ Å.

structure of the blue phosphorene. The complete image of the phosphorene quasi-bilayer thus can not be observed with the STM measurement. The primitive cell of phosphorene is highlighted by cyan circles along with the corresponding lattice vectors (purple) with a common lattice parameter of (3.7±0.1) Å. The previously recognized moire effect is clearly visible, originating from the geometrical similarity of the substrate and the superstructure. The unit cell of the resulting pattern is, as was mentioned above, showing the lattice parameter of (2.7±0.2) nm and is rotated by the angle of 30° with respect to the blue phosphorene.

3.2.3 3rd structure

In light of the predicted (and experimentally confirmed) strong layer-dependance of the crucial blue phosphorene properties, the urge of multi-layer phosphorene preparation naturally occurs. Hence, the deposition was not terminated with the single-layer blue phosphorene formation. On contrary, the deposition parameters (cell temperature, sample temperature, pressure) were left unchanged and the deposition process was continued even after the blue phosphorene formation. As is evident from the results of the LEEM experiments, long deposition times lead to the formation of new features on top of the the blue phosphorene layer.

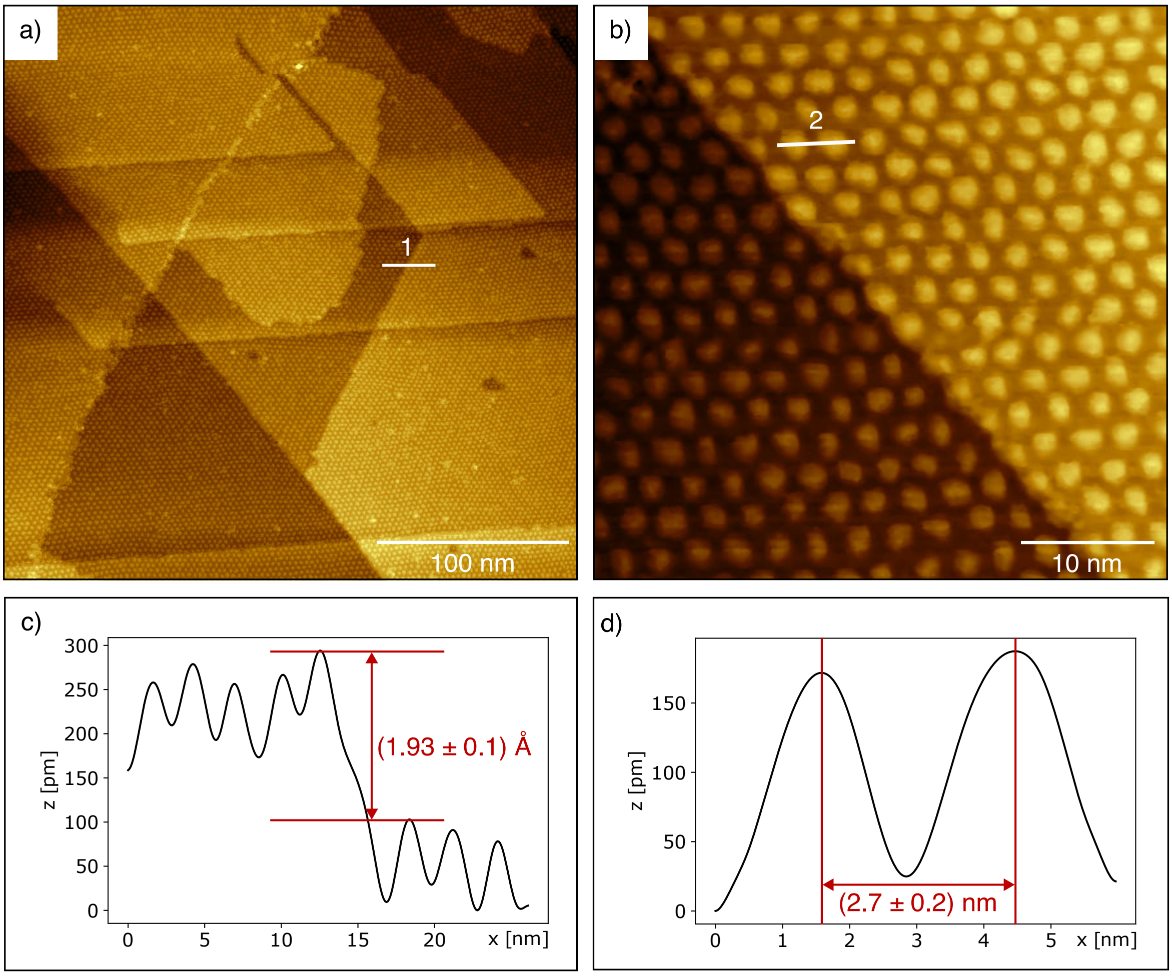

Figure 3.4: STM images of single-layer blue phosphorene formed on Cu(111): a) typical large-scale image of Cu(111) terraces covered with single-layer blue phosphorene: the structure formed on the copper substrate exhibits a clearly visible moire effect (U_{bias} = 2.0 V, $I_{setpoint}$ = 52 pA); b) closer look at the moire pattern visible on two adjacent Cu(111) terraces, showing irregularities in the shape of signal maxima (U_{bias} = -2.0 V, $I_{setpoint}$ = 52 pA); c) line profile along line 2 in a): the height of single-layer phosphorene step is (1.93 ± 0.10) Å. The value was determined by a statistical analysis of data acquired on several samples and agrees with an experimentally determined value of clean Cu(111) terrace height (2.03 ± 0.04) Å; d) line profile along line 1 in b): the lattice constant of the moire pattern was found to be (2.7 ± 0.2) nm. The value was determined by a statistical analysis of data acquired on several samples.

In accordance with the LEEM results, the large-scale STM measurements show the presence of thin quasi-triangular islands on top of the previously characterized moire pattern of the blue phosphorene. Very tall lamellar phosphorus clusters are spread all over the surface, maintaining three preferred directions. The occurrence of the tall clusters is significantly reduced with increased sample temperature during the deposition, which simultaneously leads to the formation of larger quasi-triangular islands (compare Figures 3.6 a and b).

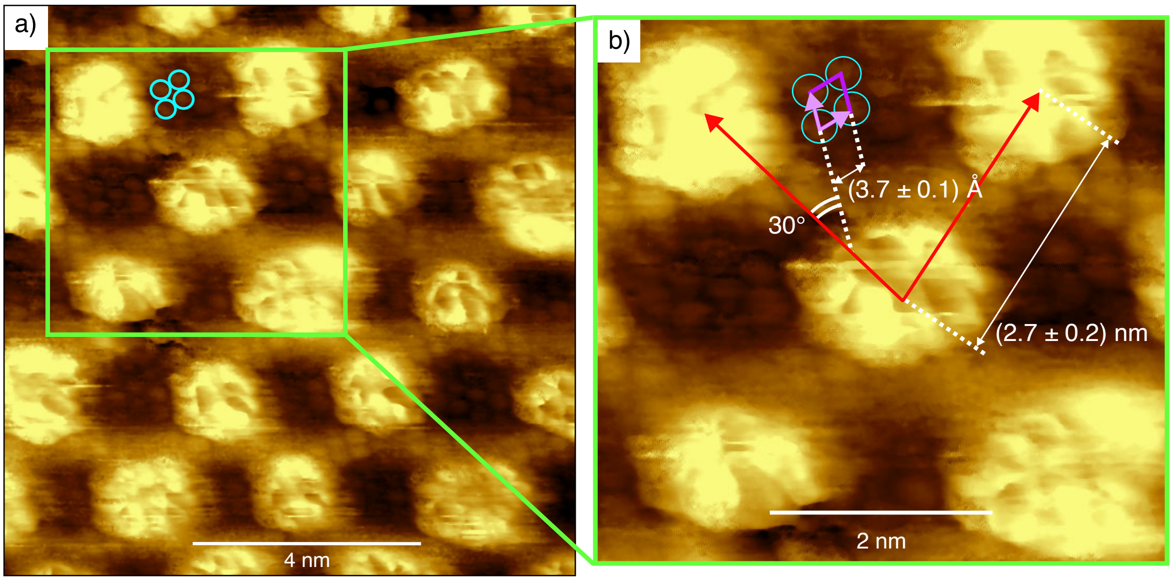

Figure 3.5: a) Atomically resolved close-up image of the surface presented in Figure 3.4 (U_{bias} = -1.3 V, $I_{setpoint}$ = 52 pA); b) zoomed-in image of the reduced area labeled in a): the moire pattern lattice (labeled with red lattice vectors with size of (2.7 ± 0.2) nm) is rotated by 30 ° with respect to the resolved lattice of phosphorene (labeled with blue circles and purple lattice vectors with size of (2.7 ± 0.1) Å).

Usually the islands do not seem to show any structural ordering and their surface thus seems to be rather amorphous. However, in several cases a highly-ordered structure was found to be formed in limited regions of the islands surface, showing an altering and almost defect-free zig-zag pattern in the STM acquisition. The quasi-topographic height level of the well ordered structure is not showing any significant increase compared to the adjacent amorphous regions. The zig-zag pattern is thus considered to be a result of a structure created by the partial island structural transformation rather than an adlayer grown on the standard island. A two-dimensional fast Fourier transform (2D FFT) processing of the image presented in Figure 3.6d results in the reciprocal space image shown in Figure 3.7a. A direct comparison with the LEEM diffraction image acquired on the corresponding sample type and showing the typical star-like pattern does not reveal any significant similarity of the two patterns. In light of this finding, the observed zig-zag structure seems to cover only a small region of the whole sample, thus leading to a small intensity of the corresponding diffraction pattern.

In order to understand the electronic properties of the grown structures, a large set of bias spectroscopy (STS) measurements was carried out on the described zigzag structure. However, the measurements were not successful since no relevant and consistent results were obtained in the dataset. An example of the obtained spectra is presented in the Figure 3.8, showing a noise with a clearly visible harmonic component. Several significant signal peaks were observed in few of the obtained spectra, the position was however not consistent and thus can not be interpreted.

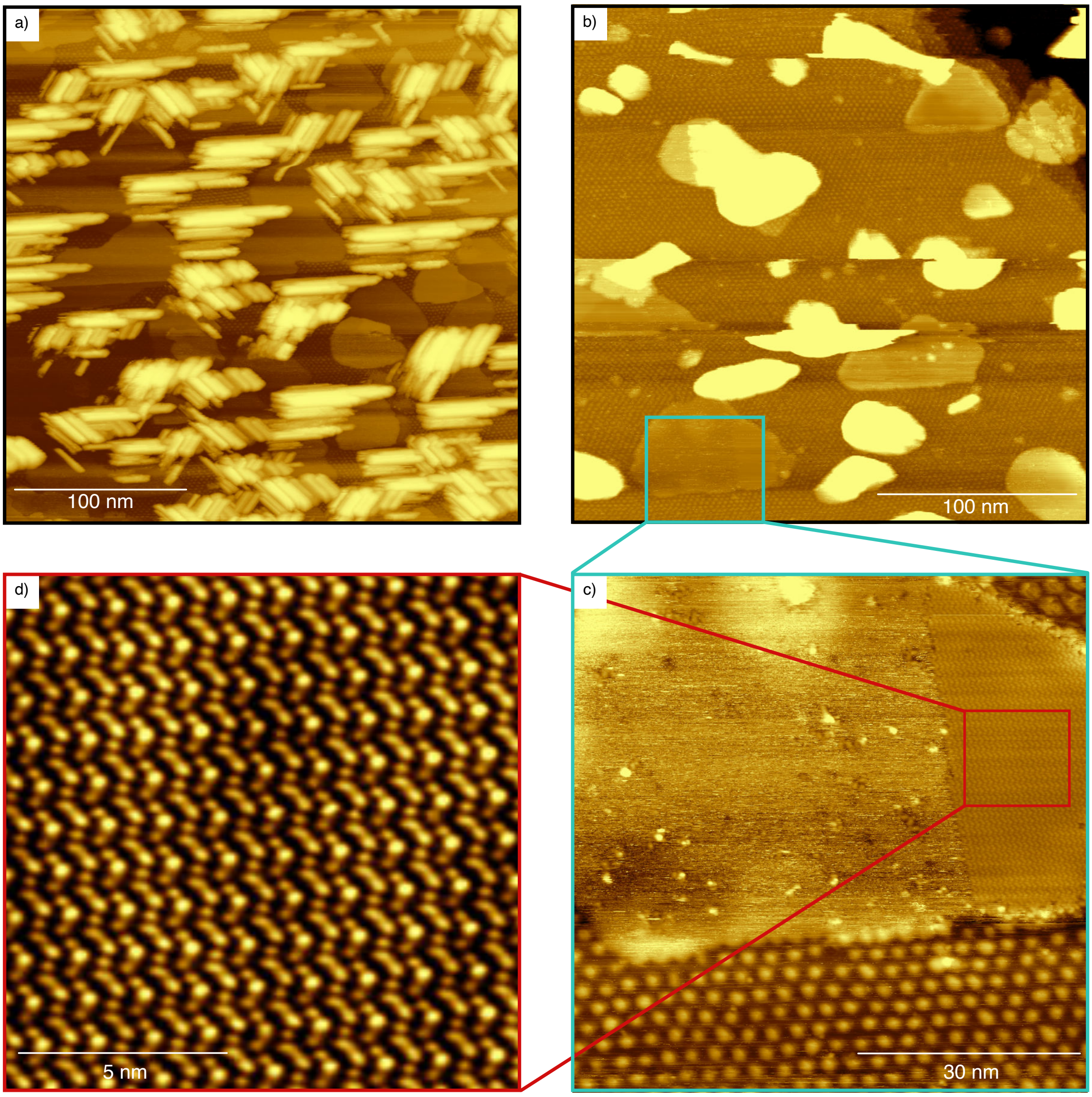

Figure 3.6: STM images of structures occurring after further phosphorus deposition on the structure described in Section 3.2.2: a) Large-scale image of the sample surface formed at 180 °C: the previously described moire structure is observed as a base layer covered with low-profile islands with no visible regular patterns on their surface. On top of the whole surface, tall quasi-linear phosphorus clusters (height of 4 to 8 nm) are grown, randomly oriented into three preferred directions ($U_{bias} = 1.2$ V, $I_{setpoint} = 50$ pA); b) high-temperature version of the structure shown in a): an increased temperature of the sample ($T = 230$ °C) during the deposition leads to the reduction of the tall clusters occurence and enlargement of the low profile islands ($U_{bias} = 2.2$ V, $I_{setpoint} = 50$ pA); c) high resolution scan of the reduced area labeled in b): a highly ordered zig-zag structure is visible in a part of the island, the rest of the island surface appears to be amorphous. No height profile step is observed between the zig-zag and the amorphous structure carrying regions ($U_{bias} = 2.2$ V, $I_{setpoint} = 50$ pA); d) atomically resolved image of the reduced area labeled in c): altering mutually mirrored quasi-linear asymmetrical-zigzag patterns are observed ($U_{bias} = 2.2$ V, $I_{setpoint} = 50$ pA).

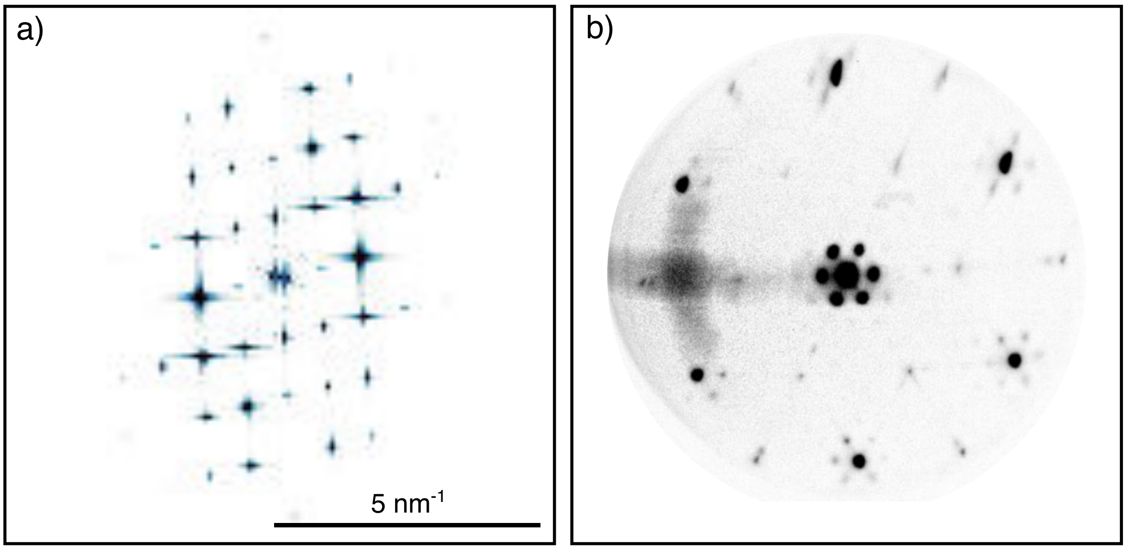

Figure 3.7: a) Figure 3.6d transformed into the reciprocal space applying 2D FFT (Fast Fourier transform) algorithm; b) LEEM diffraction pattern acquired on the same sample type: the typical star-like pattern is visible, showing no significant similarity with a).

3.3 Stability

As mentioned in the Section 1.1, blue phosphorene is predicted to be inherently susceptible to rapid degradation when exposed to oxidative atmospheric conditions. Although a study discussing the structure stability under ultra-high vacuum conditions assuring a very low concentration of the oxidation agents is missing, the knowledge of the structure behaviour in the highly clean and inert environment is crucial for a deeper understanding of the degradation mechanisms at higher pressures and represents an important step on the way to the potential future applications of the material. Here, an in-situ experiment was carried out, employing the UHV-STM technique to analyse the time-dependent degradation of the prepared structures.

The Figure 3.9 shows STM snapshots acquired during the first sixty-four hours following the deposition end. The sample was left stored in the UHV-STM chamber at the room temperature and pressure better than $1 \cdot 10^{-9}$ mbar. The initial state represents the typical surface of the 3rd structure, composed of thin quasi-triangular islands and tall amorphous phosphorus clusters grown on top of the single-layer phosphorene. No structural changes are observed 16 hours after the initial state. The first signs of degradation are visible on phosphorene 48 hours after the initial state and adopt the form of slight clusterization of its structure. The image acquired after next 16 hours already shows massive clusterization of both phosphorene and triangular islands on top of it. The amorphous phosphorus clusters do not exhibit any observable morphological changes.

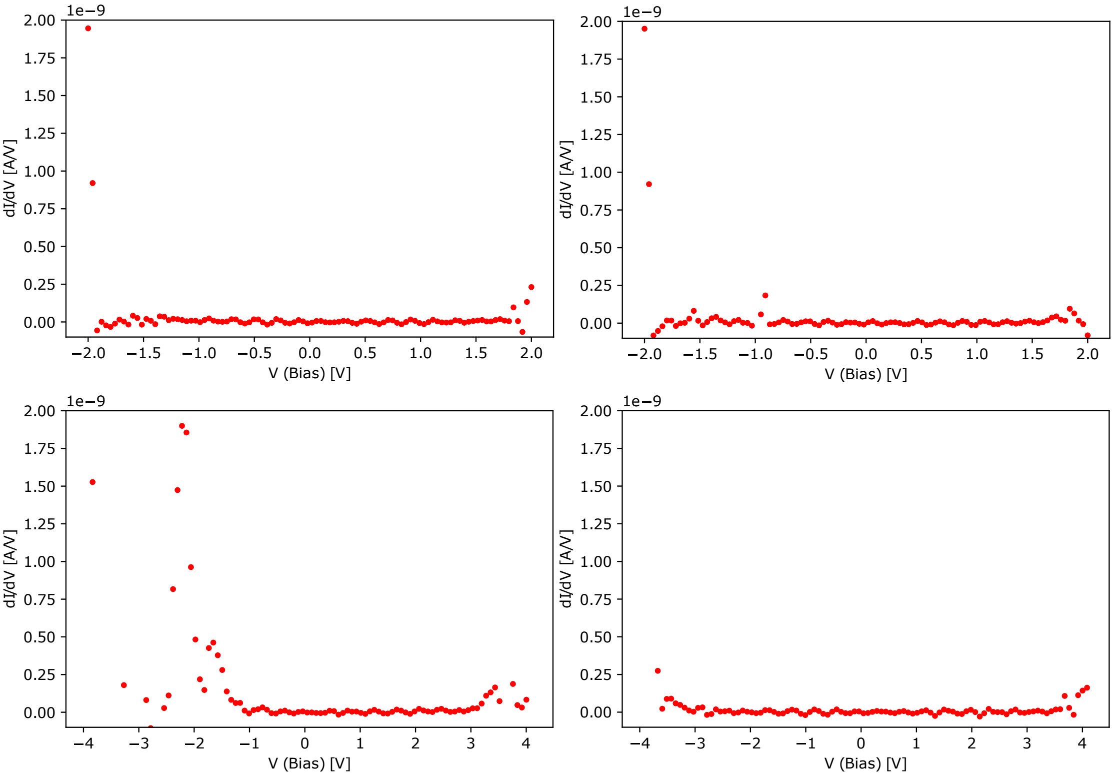

Figure 3.8: Examples of dI/dV spectra obtained by performing bias spectroscopy in various spots over the zig-zag pattern regions at V_b voltage range of (−2,+2) V and (−4,+4) V. Large number (40) of STS measurements on different spots of the sample was performed, showing no consistency in the results. Most of the dataset is indistinguishable from a noise containing harmonic component most probably originating from the lock-in amplifier. Few datasets show peaks in the high-bias regions, there is however no consistency in the maxima positions. The experiments were carried out at a room temperature and pressure lower than 10^{-10} mbar.

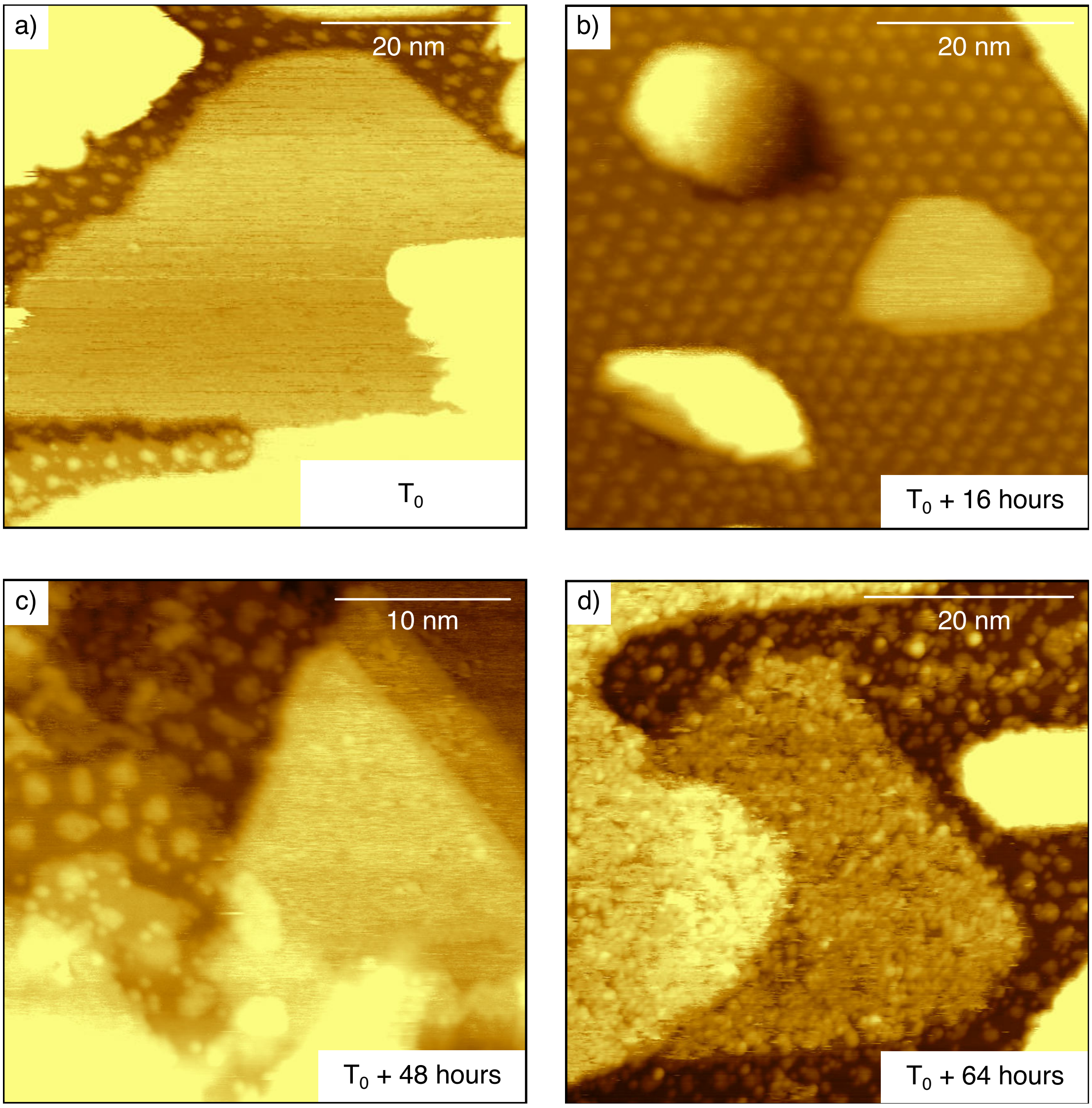

Figure 3.9: A sequence of STM images acquired on the 3rd structure during first 64 hours after the deposition. The sample was left in the SPM UHV chamber at 22 °C and pressure better than $1 \cdot 10^{-9}$ mbar: a) Image acquired immediately after the deposition (T_0). The structure appearance is consistent with a typical 3rd structure described in Section 3.2.3 (U_{bias} = 1.3 V, $I_{setpoint}$ = 52 pA); b) Image acquired 16 hours after the deposition. No changes are visible on any of the structures present (U_{bias} = 2.5 V, $I_{setpoint}$ = 55 pA); c) Image acquired 48 hours after deposition: first signs of clusterisation are visible on the corrugated moire structure, the high phosphorus clusters and thin islands do not show any significant structural changes (U_{bias} = 1.5 V, $I_{setpoint}$ = 47 pA); d) Image acquired 64 hours after the deposition: a massive clusterisation of both the moire and thin island structure is observed, no periodical arrangement can be recognized in the former moire structure and the islands have lost the compactness. The high phosphorus clusters do not show any significant changes (U_{bias} = 1.5 V, $I_{setpoint}$ = 48 pA).

Summary and Discussion

The theoretical part of the bachelor's thesis briefly introduces the black and blue phosphorene, pointing out the outstanding properties predicted for both the attractive allotropes of this promising 2D material. A systematic research on current progress in few-layer black phosphorene fabrication is presented, discussing both the classical top-down methods and modern bottom-up approaches. As was found, despite an indisputable progress made over the last few years, the fabrication of large-scale black phosphorene nanosheets of a quality sufficient for any industrial application remains a challenge. This induces an increasing motivation to study blue phosphorene which is exclusively fabricable by means of the bottom-up methods. A complex research on the current achievements in the quickly developing field of blue phosphorene synthesis was performed, taking into account the outcome of both the theoretical and experimental works. The research shows that the preparation of blue phosphorene was successfully achieved and well documented within the phosphorus deposition on a weakly interacting Au(111) substrate. The moderately interacting Ag(111) was also shown to allow the blue phosphorene growth, although only in a form of small-scale clusters. The attempts to lower the substrate-phosphorene interaction led to the experiments showing blue phosphorene growth on metals covered with low-interaction buffer layer, such as Cu_3O_2 on Cu(111) or tellurium functionalized Au(111). While the computational studies suggested the impossibility of the blue phosphorene stabilization upon the highly interacting substrates, the very recent experiments prove the opposite, showing a successful preparation of a large-scale blue phosphorene by a deposition of phosphorus on a bare Cu(111) crystal.

In the experimental section of this work, a detailed mapping of the structures formed upon the phosphorus evaporation onto a bare Cu(111) crystal is presented. Thanks to the cooperation with Bc. Jiří David who conducted the growth experiments with in-situ LEEM measurements, a detailed real-space analysis of the grown structures using the scanning tunneling microscopy could be performed. A brief summary of the in-situ LEEM experiments outcome is also included in order to build the necessary background for the hereby presented results.

Similarly to the results reported by the works employing the Au(111) and Ag(111) crystals as a substrate (Figure 3.10ab), the sub-monolayer coverage of phosphorus on Cu(111) leads to the formation of quasi-linear structures (1st structure). In constrast to the first two substrates mentioned, the structure observed on Cu(111) is apparently more compact, showing much smaller inter-chain distance. Supported by the results of the LEEM experiments, the linear structure observable in the Figure 3.10c was characterized as $(\sqrt{3} \times \sqrt{13})$R30°.

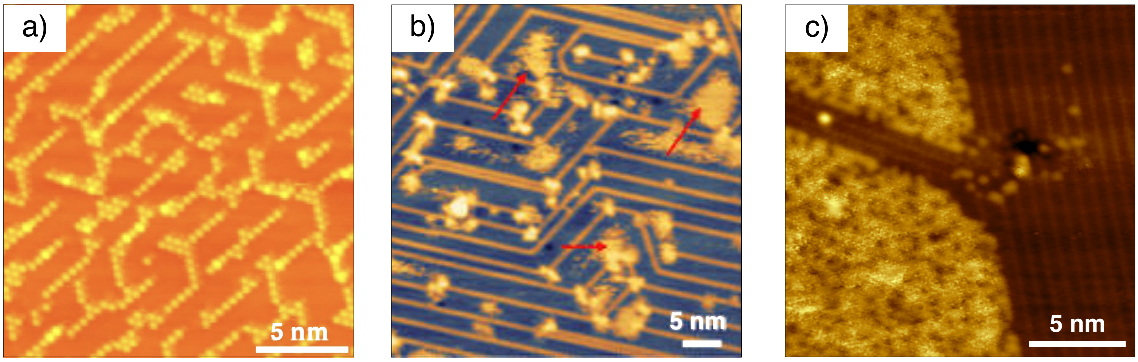

Figure 3.10: Comparison of STM images acquired on the low-coverage structures appearing upon phosphorus deposition on a)Au(111) [27], b) Ag(111) [33] and c) Cu(111). All three low-coverage structures are showing a linear chain-like phase ordered into three preferred directions.

As observed in LEEM, further deposition leads to a very fast transformation of the whole surface to a new well ordered superstructure, homogeneously covering the whole substrate surface. The STM analysis reveals large terraces covered with a homogeneous structure exhibiting a hexagonally ordered moire pattern. The atomically resolved STM image reveals the lattice parameter of (3.7±0.1) Å. This corresponds with the lattice of the blue phosphorene dilated by 10-12%, which is possible as a consequence of the significant lattice mismatch between phosphorene and the substrate and the high copper interaction strength. The resulting moire pattern lattice is rotated by 30° with respect to the actual superstructure and shows a lattice parameter of (2.7 ± 0.2) nm. Considering the constant terrace height equal to the one measured on the bare Cu(111), the 2nd grown structure is determined to be a single-layer blue phosphorene. This is in contrary to the results of Kaddar et al., who have reported the growth of single-layer (1 ML) blue phosphorene and nanodot covered single-layer blue phosphorene (1.5 ML) on Cu(111), showing the resulting pattern periodicity of 4.3 nm and 3.3 nm respectively. The reported single-layer phosphorene shows a lattice constant of 3.4 Å, which is close to the theoretical lattice constant of a free-standing blue phosphorene (3.3 Å). However, the results of this paper show significant inconsistencies in interpretation of the data (reported size of features does not match the dimensions defined by the scalebars included in the images) and, hence, the reported conclusions can not be directly compared with those revealed in this work. This being said, further investigation would need to be performed in order to clarify the inconsistencies and find a way to compare the reported results with those presented here.

Long deposition experiments were performed in order to investigate a potential formation of double-layer phosphorene. With long deposition times, new features arise on top of the phosphorene layer. The STM analysis shows a presence of thin quasi-triangular islands accompanied with tall amorphous clusters of phosphorus, both placed on top of the blue phosphorene's moire pattern. The thin islands do not usually show any well-ordered structure and thus appear to be amorphous. However some of them were found to contain regions exhibiting a highly-ordered zig-zag structure on the surface. The resulting pattern is similar (yet different if properly analysed) to the one reported within a defect-induced growth by Zhou et al., who have performed phosphorene growth experiments with Cu_3O_2 buffer layer on Cu(111) as a substrate (see Figure 3.11). In our case, the possibility of local oxidation of the Cu(111) substrate and subsequent phosphorus structure growth cannot be securely ruled out. The obtained pattern, however, shows different periodicity compared to the one revealed by Zhou et al.

In order to map the electronic properties of the grown structure, large dataset (40 independent measurements on different spots within a sample) of dI/dV STS spectra was obtained, focusing on the previously described zig-zag structure. The experiments were, however, not successful since the measured dataset does not yield a statistically relevant result. The majority of data shows a noisy background containing a harmonic component, which is probably originating from the lock-in amplifier modulation. The experiments were carried out at a room temperature, which is not ideal for the STS measurements due to the Boltzmann energy spread. Furthermore, the KolibriSensor quartz probe used for the measurements in the UHV-SPM system is widely used for acquisitions on various sample types, the requirements of the tip-condition-sensitive bias spectroscopy thus could not be fulfilled. Further experiments featuring the tunneling spectroscopy on blue phosphorene will be carried-out in order to characterize the influence of the substrate on the predicted large band gap. To ensure better results, an Ar^+ sputtering will be performed in order to sharpen the tip and the actual acquisition will be carried out at 100 K.

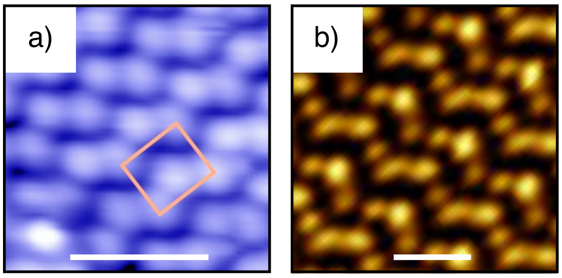

Figure 3.11: Comparison of the zig-zag structures: (a) reported to occur withing P deposition on copper oxide by Zhou et al., shows a dimeric structure [34]; (b) obtained in our experiments, shows trimeric structure. Scale bar dimension for a) and b) is 2 nm and 1 nm respectively.

Last but not least, an in-situ STM survey focusing on the stability of the grown structures was performed. The sample containing a standard 3rd structure was kept in an UHV chamber at a room temperature and pressure better than $1 \cdot 10^{-9}$ mbar for the first 64 hours following the deposition end. Consequently the STM aquisition was performed within a number of few hours long interval. The first signs of degradation are observable within the underlying 2nd structure, where a slight clusterization is visible 48 hours following the preparation. In another 16 hours, a massive clusterization proceeds, resulting with both the 2nd structure and thin islands loosing the compactness and any signs of spatial ordering. The blue phosphorene was theoretically predicted to be very sensitive for an on-air degradation, here it is shown that a substrate-connected phosphorene may not last stable even under the UHV conditions. This can be either caused by the instability of the structure itself or by the oxidation caused by the residual pressure in the chamber. However, it is confirmed that any possible future application of the otherwise exceptionally interesting material is contingent on finding a mean to stabilize it.

Bibliography

[1] Vigneshwaran Shanmugam et al. A Review of the Synthesis, Properties, and Applications of 2D Materials. In: *Particle &amp Particle Systems Characterization* 39.6 (May 2022), p. 2200031. DOI: `10.1002/ppsc.202200031`.

[2] Ömer Güler and Nihal Bağcı. A short review on mechanical properties of graphene reinforced metal matrix composites. In: *Journal of Materials Research and Technology* 9.3 (May 2020), pp. 6808–6833. DOI: `10.1016/j.jmrt.2020.01.077`.

[3] A. K. Geim and K. S. Novoselov. The rise of graphene. In: *Nature Materials* 6.3 (Mar. 2007), pp. 183–191. DOI: `10.1038/nmat1849`.

[4] Sajedeh Manzeli et al. 2D transition metal dichalcogenides. In: *Nature Reviews Materials* 2.8 (June 2017), pp. 139–143. DOI: `10.1038/natrevmats.2017.33`.

[5] Meng-Yen Tsai et al. Flexible MoSsub2/sub Field-Effect Transistors for Gate-Tunable Piezoresistive Strain Sensors. In: *ACS Applied Materials &amp Interfaces* 7.23 (June 2015), pp. 12850–12855. DOI: `10.1021/acsami.5b02336`. Available at: `https://doi.org/10.1021/acsami.5b02336`.

[6] Kailiang Zhang et al. Two dimensional hexagonal boron nitride (2D-hBN): synthesis, properties and applications. In: *Journal of Materials Chemistry C* 5.46 (2017), pp. 11992–12022. DOI: `10.1039/c7tc04300g`. Available at: `https://doi.org/10.1039/c7tc04300g`.

[7] Shahinoor Alam et al. Synthesis of emerging two-dimensional (2D) materials – Advances, challenges and prospects. In: *FlatChem* 30 (Nov. 2021), p. 100305. DOI: `10.1016/j.flatc.2021.100305`. Available at: `https://doi.org/10.1016/j.flatc.2021.100305`.

[8] Zhen Zhu and David Tománek. Semiconducting Layered Blue Phosphorus: A Computational Study. In: *Phys. Rev. Lett.* 112 (17 May 2014), p. 176802. DOI: `10.1103/PhysRevLett.112.176802`.

[9] Ankit Jain and Alan J. H. McGaughey. Strongly anisotropic in-plane thermal transport in single-layer black phosphorene. In: *Scientific Reports* 5.1 (Feb. 2015), p. 8501. DOI: `10.1038/srep08501`.

[10] Xi Ling et al. The renaissance of black phosphorus. In: *Proceedings of the National Academy of Sciences* 112.15 (2015), pp. 4523–4530. DOI: `10.1073/pnas.1416581112`.

[11] Tony Low et al. Tunable optical properties of multilayer black phosphorus thin films. In: *Phys. Rev. B* 90 (7 Aug. 2014), p. 075434. DOI: `10.1103/PhysRevB.90.075434`.

[12] Tony Low et al. Tunable optical properties of multilayer black phosphorus thin films. In: *Physical Review B* 90.7 (Aug. 2014), p. 075434. DOI: `10.1103/physrevb.90.075434`.

[13] Han Liu et al. Phosphorene: An Unexplored 2D Semiconductor with a High Hole Mobility. In: *ACS Nano* 8.4 (2014), pp. 4033–4041. DOI: `10.1021/nn501226z`.

[14] K. S. Novoselov et al. Electric Field Effect in Atomically Thin Carbon Films. In: *Science* 306.5696 (2004), pp. 666–669. DOI: `10.1126/science.1102896`.

[15] Yuan Huang et al. Universal mechanical exfoliation of large-area 2D crystals. In: *Nature Communications* 11.1 (May 2020), p. 2453. DOI: `10.1038/s41467-020-16266-w`.

[16] Jack R. Brent et al. Production of few-layer phosphorene by liquid exfoliation of black phosphorus. In: *Chem. Commun.* 50.87 (2014), pp. 13338–13341. DOI: `10.1039/c4cc05752j`.

[17] Zhe Yan et al. Solvothermal-assisted liquid-phase exfoliation of large size and high quality black phosphorus. In: *Journal of Materiomics* 4.2 (June 2018), pp. 129–134. DOI: `10.1016/j.jmat.2018.01.003`.

[18] Munkhjargal Bat-Erdene et al. Efficient and Fast Synthesis of Few-Layer Black Phosphorus via Microwave-Assisted Liquid-Phase Exfoliation. In: *Small Methods* 1.12 (Nov. 2017), p. 1700260. DOI: `10.1002/smtd.201700260`.

[19] Amin Rabiei Baboukani et al. Liquid-Based Exfoliation of Black Phosphorus into Phosphorene and Its Application for Energy Storage Devices. In: *Small Structures* 2.5 (Jan. 2021), p. 2000148. DOI: `10.1002/sstr.202000148`.

[20] Joshua B Smith, Daniel Hagaman, and Hai-Feng Ji. Growth of 2D black phosphorus film from chemical vapor deposition. In: *Nanotechnology* 27.21 (Apr. 2016), p. 215602. DOI: `10.1088/0957-4484/27/21/215602`.

[21] Zehan Wu et al. Large-scale growth of few-layer two-dimensional black phosphorus. In: *Nature Materials* 20.9 (May 2021), pp. 1203–1209. DOI: `10.1038/s41563-021-01001-7`.

[22] Yijun Xu et al. Epitaxial nucleation and lateral growth of high-crystalline black phosphorus films on silicon. In: *Nature Communications* 11.1 (Mar. 2020), p. 1330. DOI: `10.1038/s41467-020-14902-z`.

[23] Jiang Zeng, Ping Cui, and Zhenyu Zhang. Half Layer By Half Layer Growth of a Blue Phosphorene Monolayer on a GaN(001) Substrate. In: *Physical Review Letters* 118.4 (Jan. 2017), p. 046101. DOI: `10.1103/physrevlett.118.046101`.

[24] Jia Lin Zhang et al. Epitaxial Growth of Single Layer Blue Phosphorus: A New Phase of Two-Dimensional Phosphorus. In: *Nano Letters* 16.8 (July 2016), pp. 4903–4908. DOI: `10.1021/acs.nanolett.6b01459`.

[25] Chengding Gu et al. Growth of Quasi-Free-Standing Single-Layer Blue Phosphorus on Tellurium Monolayer Functionalized Au(111). In: *ACS Nano* 11.5 (May 2017), pp. 4943–4949. DOI: `10.1021/acsnano.7b01575`.

[26] V. I. Gorbenko and A. N. Gorban. Thermal decomposition of indium phosphide in vacuum and atomic hydrogen environment. In: *Radio Electronics, Computer Science, Control* 0.1 (July 2012), pp. 7–10. DOI: `10.15588/1607-3274-2012-1-1`.

[27] Jin-Peng Xu et al. One-dimensional phosphorus chain and two-dimensional blue phosphorene grown on Au(111) by molecular-beam epitaxy. In: *Physical Review Materials* 1.6 (Nov. 2017), p. 061002. DOI: `10.1103/physrevmaterials.1.061002`.

[28] Wei Zhang et al. Epitaxial Synthesis of Blue Phosphorene. In: *Small* 14.51 (Oct. 2018), p. 1804066. DOI: `10.1002/smll.201804066`.

[29] Yuling Yin et al. Stabilities of Isomers of Phosphorus on Transition Metal Substrates. In: *Chemistry of Materials* 33.23 (Dec. 2021), pp. 9447–9453. DOI: `10.1021/acs.chemmater.1c03489`. Available at: `https://doi.org/10.1021/acs.chemmater.1c03489`.

[30] Jia Lin Zhang et al. Synthesis of Monolayer Blue Phosphorus Enabled by Silicon Intercalation. In: *ACS Nano* 14.3 (Mar. 2020), pp. 3687–3695. DOI: `10.1021/acsnano.0c00822`.

[31] Yuling Yin et al. Phosphorus Chains and Pentamers: The Precursors of Blue Phosphorene on the Ag(111) Substrate. In: *Chemistry of Materials* 34.18 (Sept. 2022), pp. 8230–8236. DOI: `10.1021/acs.chemmater.2c01543`.

[32] Shuo Yang et al. Regular Arrangement of Two-Dimensional Clusters of Blue Phosphorene on Ag(111). In: *Chinese Physics Letters* 37.9 (Sept. 2020), p. 096803. DOI: `10.1088/0256-307x/37/9/096803`.

[33] Yihe Wang et al. Evolution of Low-Dimensional Phosphorus Allotropes on Ag(111). In: *Chemistry of Materials* 34.23 (Nov. 2022), pp. 10651–10658. DOI: `10.1021/acs.chemmater.2c02812`.

[34] Dechun Zhou et al. Epitaxial Growth of Flat, Metallic Monolayer Phosphorene on Metal Oxide. In: *ACS Nano* 14.2 (Feb. 2020), pp. 2385–2394. DOI: `10.1021/acsnano.9b09588`.

[35] Youness Kaddar et al. Dirac Fermions in Blue Phosphorene Monolayer. In: *Advanced Functional Materials* (Feb. 2023), p. 2213664. DOI: `10.1002/adfm.202213664`.

[36] Gaoxue Wang et al. Degradation of phosphorene in air: understanding at atomic level. In: *2D Materials* 3.2 (Apr. 2016), p. 025011. DOI: `10.1088/2053-1583/3/2/025011`.

[37] *Ultra High Vacuum Preparation and Analytical System (UHV-CLUSTER).* [online] Accessed 2023-02-19. Available at: `https://nano.ceitec.cz/ultra-high-vacuum-preparation-and-analytical-system-uhv-cluster/`.

[38] *GAP DECOMPOSITION SOURCE DECO data sheet.* [online], Accessed 2023-04-02. Available at: `https://www.mbe-komponenten.de/products/mbe-components/effusion-cells/deco.php`.

[39] E Bauer. Low energy electron microscopy. In: *Reports on Progress in Physics* 57.9 (Sept. 1994), pp. 895–938. DOI: `10.1088/0034-4885/57/9/002`.

[40] Ke Bian et al. Scanning probe microscopy. In: *Nature Reviews Methods Primers* 1.1 (May 2021), p. 36. DOI: `10.1038/s43586-021-00033-2`.

[41] Donald M Eigler and Erhard K Schweizer. Positioning single atoms with a scanning tunnelling microscope. In: *Nature* 344 (1990), pp. 524–526.

[42] Shigemitsu Nakanishi and Tetsuo Horiguchi. Surface Lattice Constants of Si(111), Ni(111) and Cu(111). In: *Japanese Journal of Applied Physics* 20.3 (Mar. 1981), p. L214. DOI: `10.1143/jjap.20.l214`.

Abbreviations

1D

one-dimensional. 9, 10

2D

two-dimensional. 3–5, 7, 14, 19, 26, 28, 30, 33

AFM

Atomic-force microscopy. 18, 20

CVD

Chemical vapor deposition. 3, 6

DFT

Density-functional theory. 7, 8, 10

DOS

Density of states. 19, 20

FFT

Fast Fourier transform. 28, 30

FM-AFM

Frequency modulation atomic-force microscopy. 20

FTIR

Fourier transform infrared spectroscopy. 15

hBN

Hexagonal boron nitride. 3

LEED

Low-energy electron diffraction. 12, 15, 16

LEEM

Low-energy electron microscopy. 4, 15–18, 22, 23, 26–28, 30, 33, 34

LEIS

Low-energy ion scattering spectroscopy. 15, 16

MBE

Molecular beam epitaxy. 10, 15, 16

PES

Photoemission spectroscopy. 8, 12, 13, 15

PLD

Pulsed laser deposition. 6, 7, 15

PREP

Preparation chamber. 15

PVD

Physical vapor deposition. 3

RHEED

Reflection high-energy electron diffraction. 15

SEM

Scanning electron microscopy. 17

SPM

Scanning-probe microscopy. 15, 18, 32, 35

STM

Scanning tunneling microscopy. 4, 9–13, 19, 20, 22, 24–30, 32, 34, 35

STS

Scanning tunneling spectroscopy. 4, 12, 20, 28, 31, 35

TEM

Transmission electron microscopy. 16, 17

TMDs

Transition metal dichalcogenides. 3

UHV

Ultra-high vacuum. 14, 15, 30, 32, 35

XPS

X-ray photoelectron spectroscopy. 16